

GPR analysis of clayey soil behaviour in unsaturated conditions for pavement engineering and geoscience applications

Tosti, Fabio; Benedetto, A; Bianchini Ciampoli, Luca; Lambot, S.; Patriarca, Claudio; Slob, Evert

DOI

[10.3997/1873-0604.2016011](https://doi.org/10.3997/1873-0604.2016011)

Publication date

2016

Document Version

Accepted author manuscript

Published in

Near Surface Geophysics

Citation (APA)

Tosti, F., Benedetto, A., Bianchini Ciampoli, L., Lambot, S., Patriarca, C., & Slob, E. (2016). GPR analysis of clayey soil behaviour in unsaturated conditions for pavement engineering and geoscience applications. *Near Surface Geophysics*, 14(2), 127-144. <https://doi.org/10.3997/1873-0604.2016011>

Important note

To cite this publication, please use the final published version (if applicable). Please check the document version above.

Copyright

Other than for strictly personal use, it is not permitted to download, forward or distribute the text or part of it, without the consent of the author(s) and/or copyright holder(s), unless the work is under an open content license such as Creative Commons.

Takedown policy

Please contact us and provide details if you believe this document breaches copyrights. We will remove access to the work immediately and investigate your claim.

GPR analysis of clayey soil behavior in unsaturated conditions for pavement engineering applications

Fabio Tosti^{1,*}, Andrea Benedetto¹, Luca Bianchini Ciampoli¹, Sébastien Lambot², Claudio Patriarca³, Evert C. Slob⁴

¹Department of Engineering, Roma Tre University, Via Vito Volterra 62, 00146, Rome, Italy; e-mail: fabio.tosti@uniroma3.it; andrea.benedetto@uniroma3; bianchini.ciampoli@gmail.com

²Earth and Life Institute, Environmental Sciences Université catholique de Louvain (UCL) Croix du Sud 2 box L7.05.02, 1348 Louvain-la-Neuve, Belgium; sebastien.lambot@uclouvain.be

³Statoil ASA, Sandsliveien 90, 5254 Sandsli, Norway; claudio.patriarca@gmail.com

⁴Delft University of Technology, Faculty of Civil Engineering and Geosciences, Section of Applied Geophysics and Petrophysics Department of Geoscience & Engineering, Stevinweg 1, Delft 2628 CN, The Netherlands; e.c.slob@tudelft.nl

* Corresponding author: mail: fabio.tosti@uniroma3.it; tel: +39 0657333543

Abstract

In pavement engineering, clay content is one of the primary cause of both deep and surface damages, such as subgrade failures, cracks and pavement rutting, thereby playing a crucial role in road safety issues as an indirect cause of accidents. In this paper, several ground-penetrating radar (GPR) methods and techniques have been used to non-destructively investigate the behavior of sub-asphalt compacted clayey layers and subgrade soils in unsaturated conditions. Typical road materials employed for load-bearing layers construction, classified as A1, A2 and A3 by the American Association of State Highway and Transportation Officials (AASHTO) soil classification system, were used for the laboratory tests. Clayless and clay-rich soil samples were manufactured and adequately compacted in electrically and hydraulically isolated formworks, and variable moisture conditions from dry to saturated were increasingly reached. Measurements were carried out for each water content using a pulsed radar system with ground-coupled antennas, 500 MHz center frequency, and a vector network analyzer spanning the 1–3 GHz frequency range. Different theoretically-based methods were used for data processing. Promising insights are shown to single out the influence of clay in load-bearing layers and subgrade soils, and its impacts on their electromagnetic response at variable moisture conditions.

List of keywords

clay detection; ground-penetrating radar; soil moisture; road pavement; Rayleigh scattering;
full-waveform inversion, surface reflection method, volumetric mixing formulae

INTRODUCTION

Clay detection in soils is a key topic of research in many fields of application such as, especially, construction (Miqueleiz *et al.* 2012), pavement (Uzan 1998) and geotechnical engineering (Abusharar and Han 2011), agriculture (Robinson and Phillips 2001), and Earth sciences in general (Mahmoudzadeh *et al.* 2011). Overall, clay presence is closely related to moisture content due to its considerable swelling properties (Wuddivira *et al.* 2012), thereby exerting significant effects on the stability of soils behavior under loading.

As a rule of thumb, it is conventionally used to model the hydrodynamic behavior of plastic soils during wetting-drying cycles (Dudoignon *et al.* 2007). Richard *et al.* (2001) argued that particle arrangements along with their mineralogical nature notably affect the properties of clayey soils under compressive or drying stress cycles. More recently, Beroya *et al.* 2009 have also proved that clay minerals abundance mainly governs the cyclic behavior of silt-clay mixtures. In line with this, the authors demonstrated that montmorillonitic soils have higher cyclic strength than illitic and kaolinitic soils when considering the same clay abundance, clay mineral and/or the same value of plasticity index. Therefore, clay mineralogy and its different adhesive bond strength exerted on the boundary particles is a primary indicator of the liquefaction susceptibility of cohesive soils more than clay fraction and plasticity index. Laboratory tests are usually carried out at the fine scale to analyze the volumetric changes of clay materials in gravimetric moisture domains between liquidity and shrinkage conditions (Chertkov and Ravina 2000), although Volts and Cabidoche (1995) demonstrated how shrinkage curves and the relevant size of cracks vary with respect to the scale of investigation in the unsaturated domain. In line with this, typical drying effects in clayey soils determine the development of shrinkage cracks with related vertical prism-like structures and subsidence effects (Chertkov 2005).

In pavement engineering, several procedures have become established over years to constrain the effects of clay presence in soils for both construction and rehabilitation of transport

infrastructures. In this regard, the possibility to achieve strength improvement of clays reinforced with geogrids embedded in thin layers of sand was thoroughly discussed by Abdi *et al.* (2009). Widespread use of additives such as cement, lime, fly ash, and chemicals is also made for operations of soil treatment (Pakbaz and Alipour 2012). On the contrary, when suitable strength and deformation properties of soils cannot be ensured by excessive abundance of plastic material, extra reinforcing steel to foundations and slabs as well as earthmoving operations for removing waste materials are commonly carried out (Wood *et al.* 1995). Among the most common destructive techniques for clay investigation, core sampling relies on an undeniable accuracy. Nevertheless, a very low significance of data which can be only punctually gathered notwithstanding the long distances to be surveyed in transport engineering, represents the main drawback to be tackled. In addition, such method is invasive, expensive, and time-consuming.

As a result of the above scenario, the demand for non-destructive testing techniques (NDTs) in this field of application and beyond is more and more increasing nowadays. To cite a few, acoustic methods like FWD techniques (Benedetto *et al.* 2012a; Benedetto *et al.* 2014a) are widely used to evaluate the strength and deformation properties of clayey soils, as well methods relying on spectral analyses, such as the vis-NIR spectroscopy (Viscarra Rossel *et al.* 2009), or infrared imaging (Srasra *et al.* 1994) of soil materials. Nevertheless, most of these NDTs are not time-efficient, since they cannot be continuously implemented on the road, nor cost-effective for road inspection and maintenance. Amongst the main electromagnetic (EM) methods fit for purposes, advanced high-resolution radiometer (AVHRR) (Odeh and McBratney 2000) and electromagnetic induction (EMI) (Triantafilis and Lesch 2005) can be considered as other very effective techniques, although the scale domain of investigation or the long time required for surveying are not completely suitable for pavement engineering applications.

Accordingly, it is therefore clear how an effective high-performance method capable to provide large-scale reliable measurements with a high spatial resolution, is required. In line with this, ground-penetrating radar (GPR) has proved to be one of the most powerful diagnostic non-

destructive tools that enables to collect data rapidly on the field (Tosti et al. 2014a; Benedetto *et al.* 2012b, Saarenketo and Scullion 2000). GPR is being increasingly employed in a range of many application areas such as planetary exploration, cultural heritage protection, Earth sciences, and engineering applications. Basically, this instrument allows to infer the physical conditions of subsurface relying on the transmission/reception of short electromagnetic (EM) impulses in a given frequency band (Slob *et al.* 2010; Daniels *et al.* 2004; Van der Kruk and Slob 2004).

GPR was firstly used in traffic infrastructure surveys in the first half of 1970s by the Federal Highway Administration (FHWA) for testing in tunnel applications (Morey 1998). The main applications in this field can range from physical to geometrical inspections of pavement layers. They broadly include the evaluation of layer thicknesses (Al-Qadi and Lahouar 2004), the assessment of damage conditions in HMA layers (Benedetto 2013, Scullion *et al.* 1994), load-bearing layers and subgrade soils (Benedetto and Tosti 2013a), the inspection of concrete structures (Huston *et al.* 1999, Benedetto *et al.* 2012c). New frontiers on the use of GPR in pavement engineering have been also recently tackled on the possibility to infer mechanical properties of road pavements and materials from their EM characteristics (Benedetto and Tosti 2013a; Tosti *et al.* 2014b). In addition, FDTD simulation-based approaches of the GPR signal have been recently implemented for analysing the GPR responses of typical scenarios of pavement faults (Tosti and Umiliaco 2014; Benedetto *et al.* 2014b).

More specifically on the topics of this research, many studies in the literature have been devoted to water content evaluation (Robinson *et al.* 2008). Applications in this field can be broadly classified according to the type of pavement and construction material, whereby different radar systems and processing techniques can be specifically employed. Concerning subsurface moisture measurements in subgrade soils, GPR can bridge the gap between high-resolution data (from $\sim 10^{-2}$ m to 10^{-1} m) by minor destructive techniques, such as capacitance probes (Wobshall 1978) and time domain reflectometry (TDR) (Fellner-Feldegg 1969), and low-resolution techniques (~ 10 m) by remote sensing investigations (Wagner *et al.* 2007), thereby ranking

effectively as an intermediate-scale technology (from $\sim 10^{-1}$ m to 1 m) (Lambot *et al.* 2006, Minet *et al.* 2011). Several approaches exist for estimating volumetric water content (VWC) θ by GPR (Huisman *et al.* 2003). Traditionally, an estimate of relative dielectric permittivity ϵ_r is carried out, and a petrophysical relationship is then used to convert ϵ_r into θ . Amongst such expressions, the empirical equation proposed by Topp *et al.* (1980) is undoubtedly the most used for this purpose. From a theoretical point of view, θ can be also related to ϵ_r by exploiting volumetric mixing formulae, which use the volume fraction and the dielectric permittivity of each soil constituent to derive a relationship (Dobson *et al.* 1985, Roth *et al.* 1990), or the effective medium approximations (EMA) approach, which takes into account textural and structural contributions of each component on the permittivity of a composite material (Fiori *et al.* 2005).

Overall, the aforementioned methods for moisture evaluation rely on the estimates of the relative dielectric permittivity of soils, and the use of core sampling is mostly needed for calibrating the system. In this regard, research activities are increasingly being focused on the use of efficient and self-consistent techniques. Lambot *et al.* (2004) evaluated the dielectric properties of unsaturated soils at the laboratory scale by correlating the imaginary part of the dielectric permittivity and the frequency of investigation. Moreover, a Rayleigh scattering-based method has been used by Benedetto (2010) and Benedetto *et al.* (2013) for directly predicting the volumetric water content in soils, thereby enabling to avoid the use of any petrophysical relationships and calibrations of the system.

Conversely, the GPR-based detection of clay content has been mainly reflected over years in applied studies at the field scale (Gómez-Ortiz *et al.* 2010, De Benedetto *et al.* 2012) and partially at the laboratory scale (Saarenketo 1998). More recently, several clay-dedicated laboratory studies have been specifically developed for high-resolution estimates on different textured soil materials using several self-consistent processing techniques and radar systems (Benedetto and Tosti 2013b, Patriarca *et al.* 2013, Tosti *et al.* 2013).

METHODOLOGY AND OBJECTIVES

In this paper, it is analyzed the ability of GPR to detect clay in different types of textured soils at variable moisture content conditions by using several signal processing techniques. In particular, three types of soils classified by the American Association of State Highway and Transportation Officials (AASHTO 2011) as A1, A2, and A3 were used for laboratory testing. To single out the electromagnetic behavior of the above materials relative to clay presence, clayless and clay-rich conditions amounting to 15% by weight were manufactured. The consistency of results was validated through permittivity-based methods, namely, the full-waveform inversion method, the surface reflection method, and the volumetric mixing formulae. In addition, a Rayleigh scattering-based method working in the frequency domain of the radar signal was also employed for the analyses.

The possibility to detect clay in load-bearing layers and subgrade soils for preventing structural failures of pavements and restraining the risk of severe damage can be considered as the main task of this paper, as part of an important countermeasure in quality control, rehabilitation, and maintenance operations made in transport infrastructures for improving transport safety conditions.

More specifically, the aforementioned processing techniques have been applied on data collected from samples with compacted loose materials, representing conditions from load-bearing layers and subgrade soils, which were investigated using different GPR systems.

THEORETICAL BACKGROUND

Full-Waveform Inversion Technique

The radar model

In the study proposed by Lambot *et al.* (2004), the authors proposed an intrinsic far-field antenna model concerning a planar layered medium where a local plane wave field distribution is assumed for the backscattered field over the antenna aperture. Therefore, the antenna radiation properties can be described by an equivalent single electric dipole approximation. In

such system, the wave propagation between the source point and the radar transmission line reference plane can be retrieved, on the basis of the linearity of Maxwell's equation, by means of complex, frequency-dependent global reflection and transmission coefficients. These coefficients affect the antenna and transmission line internal transmission and reflection, thereby including the antenna-medium interactions. Equation (1) describes the relationship between the radar-measured field and the 3D layered medium Green's function in the frequency domain (Lambot *et al.* 2004):

$$S_{11}(\omega) = \frac{a(\omega)}{b(\omega)} = R_i(\omega) + \frac{T(\omega)G_{xx}^\dagger(\omega)}{1-R_s(\omega)G_{xx}^\dagger(\omega)} \quad (1)$$

with $S_{11}(\omega)$ representing the raw radar signal as the ratio between the backscattered field $b(\omega)$ and incident field $a(\omega)$ at the radar transmission line reference plane, and ω describing the angular frequency. $R_i(\omega)$ stands for the global reflection coefficient of the antenna in free space, while $T(\omega) = T_i(\omega)T_s(\omega)$ with $T_i(\omega)$ is the global transmission coefficient for fields incident from the radar reference plane onto the source point, and $T_s(\omega)$ represents the global transmission coefficient for fields incident from the field point onto the radar reference plane. $R_s(\omega)$ stands for the global reflection coefficient for the field incident from layered medium onto the field point, and $G_{xx}^\dagger(\omega)$ is the layered medium Green's function. Such function is defined as the scattered x -directed field $E_x(\omega)$ at the field point for a unit-strength x -directed electric source $J_x(\omega)$ at the source point, and it can be theoretically written as (Slob and Fokkema 2002):

$$G_{xx}^\dagger(\omega) = \frac{1}{4} \int_0^\infty \tilde{G}_{xx}(k_p, \omega) dk_p \quad (2)$$

$$\tilde{G}_{xx}(k_p, \omega) = \left(\frac{\Gamma_n^{RTM}}{\eta_n} - \frac{\xi_n^{RTE}}{\Gamma_n} \right) \exp(-2\Gamma_n h_n) \quad (3)$$

where subscript TM and TE stand, respectively, for transverse magnetic mode and transverse electric mode. The R coefficients describe the reflected part of the wave in each mode.

$\Gamma_n = \sqrt{k_p^2 + \xi_n \eta_n}$ is the vertical wave number, where subscript n represents the number of

layers, $\eta_n = \sigma_n + j\omega\varepsilon_n$ and $\xi_n = j\omega\mu_n$. The global TM-mode and TE-mode reflection coefficients at the n interface are given by:

$$R^{TM} = \frac{r_{n+1}^{TM} + R_{n+1}^{TM} \exp(-2\Gamma_{n+1}h_{n+1})}{1 + r_n^{TE} + R_{n+1}^{TM} \exp(-2\Gamma_{n+1}h_{n+1})} \quad (4)$$

$$\gamma^{TM} = \frac{\eta_{n+1}\Gamma_n - \eta_n\Gamma_{n+1}}{\eta_{n+1}\Gamma_n + \eta_n\Gamma_{n+1}} \quad (5)$$

$$R^{TE} = \frac{r_{n+1}^{TE} + R_{n+1}^{TE} \exp(-2\Gamma_{n+1}h_{n+1})}{1 + r_n^{TE} + R_{n+1}^{TE} \exp(-2\Gamma_{n+1}h_{n+1})} \quad (6)$$

$$\gamma^{TE} = \frac{\mu_{n+1}\Gamma_n - \mu_n\Gamma_{n+1}}{\mu_{n+1}\Gamma_n + \mu_n\Gamma_{n+1}} \quad (7)$$

The antenna factors $R_i(\omega)$, $R_s(\omega)$ and $T(\omega)$ can be determined through a proper calibration of the antenna, consisting in the evaluation of the raw radar signal $S_{11}(\omega)$ in particular antenna-medium configurations, for which the value of the Green's function is known (e.g., measurements with the antenna at different heights over a copper sheet). In particular the $R_i(\omega)$ coefficient, i.e., the global reflection of the antenna in free space, can be defined by performing a radar measure with the antenna pointed toward the sky. It is worth noting that once the antenna factors are determined, they can be considered as constants regardless from the type of medium investigated. Accordingly, they can be filtered out from the raw signal data in order to retrieve the value of the Green's function $G_{xx}^\dagger(\omega)$.

Model inversion and objective function

Basically, this method relies on a comparison between the value of the Green's function measured on the test samples $G_{xx,meas}^\dagger(\omega)$ and the value of a theoretically modeled Green's function $G_{xx,mod}^\dagger(\omega)$, retrieved through the aforementioned theoretical assumptions.

It is therefore possible to model the behavior of the Green's function depending on fixed electromagnetic and geometrical parameters, such as the relative dielectric permittivity ϵ_r , the electrical conductivity σ , the wave number k_p , the number of layers n illuminated by the EM wave, the thickness h_n of the n layer, and the distance h_0 from the antenna aperture to the surface of the investigated medium. In this study, a mono-layered configuration as well as a fixed distance of 0.32 m between the soil sample surface and the antenna aperture are considered.

It is then possible to build a field of dielectric parameters values, sized $[N \times M]$, with N and M being, respectively, the dimensions of dielectric permittivity and electrical conductivity vectors taken into account. Accordingly, a 3D matrix of Green's function $G_{xx,mod}^\dagger(\omega)$ values can be produced in the evaluated frequency range, with dimensions $[N \times M \times F]$, where $F = B/f_s$ is the number of collected frequencies, being B and f_s , respectively, the frequency bandwidth and the frequency step selected.

The inversion process consists, basically, in retrieving the dielectric parameters ϵ_r and σ of the analyzed materials starting from the measured radar data, expressed in terms of $G_{xx,mea}^\dagger(\omega)$ rather than $S_{11}(\omega)$, and from the theoretically expected behavior of the modeled Green's function $G_{xx,mod}^\dagger(\omega)$. These two unknown values are returned through a search for the best matching between measured and modeled Green's function. In this regard, by defining a vector $\mathbf{b} = [\sigma, \epsilon_r]$, the wanted value of \mathbf{b} is the one minimizing an objective function $\varphi(\mathbf{b})$ expressing the error between measured and modeled Green's functions. In this study, the above objective function is computed as follows:

$$\varphi(\mathbf{b}) = \sqrt{\frac{\sum_{f \min}^{f \max} |G_{xx,mea} - G_{xx,mod}^{(\mathbf{b})}|^2}{\sum_{f \min}^{f \max} |G_{xx,mea}|^2}} \quad (8)$$

Frequency dependence of conductivity

In the ground-penetrating radar frequency range, a frequency-dependent behavior of the material conductivity has been detected in literature. This is mainly due to relaxation mechanisms and Maxwell-Wagner effects in the soils. In this regard, it is worth mentioning the linear relationship between σ and f proposed by Lambot *et al.* (2004):

$$\sigma(f) = \sigma_{f_i} + a(f - f_i) \quad (9)$$

where σ_{f_i} is the reference value of conductivity at the starting frequency f_i , which can be evaluated through the inversion process, and a is the variation rate of the $\sigma(f)$. Therefore, when considering σ_{f_i} variable in the range $[10^{-1} \div 10^{-4} \text{ Sm}^{-1}]$, the parameters affecting the objective function must be taken into account in a new vector $\mathbf{b} = [\sigma_{f_i}, a, \varepsilon_r]$. Typical values of a lie in the range $[10^{-10} \div 10^{-12} \text{ Ssm}^{-1}]$. In this work, a constant value of a equals to $1 \times 10^{-10} \text{ Ssm}^{-1}$ is adopted, so that the sizes of vector \mathbf{b} are related only with the two dielectrics.

Implementing the Full-waveform inversion method with the Time Domain Signal Picking approach

This approach has been adopted according to the results from Tosti *et al.* (2013), wherein laboratory tests were carried out on soil samples having the same dimensions as those used in this work. In particular, a good effectiveness was proved in forecasting dielectric permittivity values by estimating the two-way travel time of the measured radar signal within the medium. Therefore, the application of an Inverse Fast Fourier Transform (IFFT) leads to convert the domain of the signal measured from spectral into time. Once having the transformed signal

$g_{xx,mea}^{\dagger}(t)$, the time delay Δt between the air-medium and the medium-PEC reflections can be measured, by knowledge of the thickness r of the formworks, and the wave velocity through the medium v estimated by $v = 2r/\Delta t$. It is therefore possible to retrieve the value of permittivity by letting $\epsilon_{TDSP} = (c/v)^2$, where c is the speed of light in free space. From now on, such approach will be referred to as the Time Domain Signal Picking (TDSP) technique. Figure 1 shows a typical scenario of measured signal where the two above mentioned peaks of reflection are clearly identified.

FIGURE 1. Measured Green's function in the time domain $g_{xx,mea}^{\dagger}(t)$ and time delay Δt between air-medium and medium-PEC interfaces.

The implementation of the TDSP technique within a Full-waveform inversion (FWI) approach subsequently foresees to retrieve a first approximation value of dielectric permittivity ϵ_{TDSP} for each sample. As represented in the flowchart of Figure 2, this value can be therefore used as a starting point for a deeper analysis in the spectral domain, to be further refined for retrieving information about the other EM properties. The conventional FWI approach is then employed over a significant range of dielectric permittivity values, in the neighborhood of the value retrieved by the TDSP approach, namely, within the range $\pm 10\%$ of the ϵ_{TDSP} value.

FIGURE 2. Flowchart representing the implementation of the TDSP technique within a FWI approach.

Surface Reflection Method

The use of the Surface Reflection Method (SRM) leads to the evaluation of the relative dielectric permittivity of a mono-layered system by comparing the amplitude of the air-soil interface reflection and the amplitude from the air- PEC interface, taken as a reference. Such approach is commonly employed with high-frequency off-ground GPR systems. (Davis and Annan 2002, Serbin and Or 2004).

When considering a soil characterized by a certain value of permittivity ϵ_r , the reflection coefficient R at the surface separating air and soil layers can be determined as follows (Redman *et al.* 2002):

$$R = \frac{1 - \sqrt{\epsilon_r}}{1 + \sqrt{\epsilon_r}} \quad (10)$$

where 1 is the value of dielectric permittivity of the air. Equation (10) relies on the twofold assumptions of *i*) a negligible conductivity and *ii*) a simplified scenario of air layer over a homogeneous half space. By considering that the magnitude of the R coefficient at a given height position h above the surface can be also expressed as the ratio between the amplitude A_r of the reflection from the ground surface to the amplitude A_m of the reflection over a copper shield or a metal plate (with a reflection coefficient of -1), both measured at the same height h from the ground, it is possible to calculate the permittivity of the soil as:

$$\epsilon_r = \left(\frac{1 + \frac{A_r}{A_m}}{1 - \frac{A_r}{A_m}} \right)^2 \quad (11)$$

Such approach has the main advantage to provide an estimation of the soil permittivity regardless from the need for knowing any reflector position in the subsurface or the wave propagation velocity through the medium, such as in case of TDSP applications. Nevertheless, it is of evidence how an inhomogeneous water distribution within the medium could lead to different results depending on the method applied. Indeed, for higher particle-sized materials, a gravimetric behavior is prevalent for the water, which tends to stratify at the bottom as a water table. This moisture content clearly influences results of FWI or TDSP methods, while it could be neglected by SRM if the water table is too deep with respect to the air-soil interface. Many

literature studies can be cited about the capability of the SRM to sense water content on the basis of soil physical properties. Huisman *et al.* (2003) considered such influence as relevant up to depths of 20 cm. Conversely, Serbin and Or (2004) narrowed the reliability of this method to the first 1 cm below the soil surface. Therefore, it seems clear how this uncertainty can be considered as the main drawback of the SRM. Further drawbacks include a high dependence of this technique on surface roughness, along with a high sensitivity to moisture for lower water contents (Davis *et al.* 1994). On other hand, it is also worth citing the remarkable advantage of a significant lightness in computational requirements by applying the SRM approach.

Volumetric Mixing Formulae

Volumetric Mixing Formulae (VMF) rely on the volumetric fraction and the dielectric permittivity of each component of a multi-phase medium, and enable to assess the volumetric water content θ (Dobson *et al.* 1985, Roth *et al.* 1990).

By considering an n -phase medium, the general expression of a VMF can be written as follows:

$$\varepsilon_r^\alpha = \sum_{i=1}^n f_i \varepsilon_{r,i}^\alpha \quad (12)$$

where α represents a geometrical fitting parameter depending on the inner structure of the media (Lichtenecker and Rother 1931), while f_i and $\varepsilon_{r,i}^\alpha$ stand, respectively, for the volume fraction and the dielectric permittivity of the i^{th} component. By implementing Equation (12) on a three-phase system and by knowledge of the porosity φ of the soil material, it is therefore possible to determine the permittivity of the medium:

$$\varepsilon_r = (\theta \varepsilon_w^\alpha + (1 - \varphi) \varepsilon_s^\alpha + (\varphi - \theta) \varepsilon_a^\alpha)^{1/\alpha} \quad (13)$$

where ε_w^α , ε_s^α and ε_a^α are, respectively, the permittivity of free water, of the solid matrix and of the gaseous phase, and θ stands for the volumetric water content of the multi-phase system. According to this, the permittivity of the solid matrix can be evaluate by considering the relative permittivity of the multi-phase medium in dry conditions $\varepsilon_r^{\text{dry}} (\theta = 0)$, as follows (Patriarca *et al.* 2013):

$$\varepsilon_s = \left[\frac{(\varepsilon_r^{dry})^\alpha - \varphi}{1 - \varphi} \right]^{1/\alpha} \quad (14)$$

In case of clayey soils, it is necessary to consider a four-phase medium and, accordingly, a VMF expressed as follows (Roth *et al.* 1990):

$$\varepsilon_r = (\theta \varepsilon_w^\alpha + (1 - \varphi - f_c) \varepsilon_s^\alpha + (\varphi - \theta_v) \varepsilon_a^\alpha + f_c \varepsilon_c^\alpha)^{1/\alpha} \quad (15)$$

where f_c and ε_c^α stand for the volumetric clay content and the permittivity of the clay, respectively. In addition, the permittivity of the soil matrix can be determined by considering the dry conditions of the system (Patriarca *et al.* 2013):

$$\varepsilon_s = \left[\frac{(\varepsilon_r^{dry})^\alpha - \varphi - f_c \varepsilon_c^\alpha}{1 - \varphi - f_c} \right]^{1/\alpha} \quad (16)$$

In this paper, values of ε_r^{dry} were retrieved from the work of Tosti *et al.* 2013, wherein laboratory test on the same materials were carried out in dry conditions. Many efforts were devoted in the past on the value to be assigned to α , which can vary between -1 and 1. By letting $\alpha = 0.5$, it is assumed to have a wave travel time through the medium equal to the travel times within each singular component weighted by the volume (Birchak *et al.* 1974, Dobson *et al.* 1985, Gorriti and Slob 2005). Roth *et al.* (1990) proposed an α value equals to 0.46 for a three-phase medium, while Dobson *et al.* (1985) retrieved a value of 0.65 for a four-phase mixture. An interesting work has been recently developed by Patriarca *et al.* (2013), who developed a method for determining the optimal α value for different clay-rich mixtures. In this work, a value of 0.5 is adopted for the α factor.

Among the main drawbacks of this method, we can cite the need to have an a-priori knowledge of some physical properties of the multi-phase medium, as well as of the dielectric permittivity of each component.

Rayleigh Scattering Method

A recent approach relying on signal processing in the frequency domain was proposed by Benedetto (2010). Basically, the main advantage of the Rayleigh Scattering Method (RSM) falls in the not need for core sampling to calibrate the system, such that the volume fractions of the three phases in the medium are not accounted for. In this regard, θ can be directly estimated by frequency analyses of the GPR signal without estimating the dielectric permittivity. The main assumption are that in the unsaturated domain, electromagnetic waves are scattered by water droplets (Drude 1902), thereby a shifting of the frequency of the waves occurs (Bohren and Huffman 1983).

Rayleigh scattering is traditionally used to explain the shifting of the frequency of the scattered signals. A shift in the frequency distribution of the reflected signals has already been observed in the past; however, the cause of such shift was not identified or deeply investigated. Narayana and Ophir (1983) observed that different frequencies were attenuated in different media by analyzing ultrasonic waves reflected by normal and fatty livers. The authors argued that Rayleigh scattering was the primary cause of the observed non-linear behavior of the reflected waves in fatty livers. In particular, the presence of fat globules was entitled to originate Rayleigh scattering, which exhibits a fourth-order frequency dependence. More recently and with respect to another field of application, Ho *et al.* (2004) proved that buried mines with different shapes and sizes can cause a frequency shift of the signal.

Overall, it is well-known that scattering is generated by singularities or non-homogeneities in electromagnetic impedance. The process can be described as Rayleigh scattering whether the dimensions of these non-uniformities are much smaller than the wavelength of the EM wave. Analytically, the size of a scattering particle is defined by the ratio $x = 2\pi r / \lambda$, where r is the radius of the particle, and λ represents the wavelength of the signal. According to this, Rayleigh scattering occurs in the small size parameter regime when $x \ll 1$. Scattering from larger spherical particles is explained by Mie (1908) for an arbitrary size parameter x . When small values of x are considered, the Mie theory falls in the Rayleigh approximation.

By means of both several assumptions on the three-phase porous medium properties and simplifications of the physics, Benedetto (2010) defined the following formulation:

$$I(\theta_s, f) = I_0(f) \frac{1 + \cos^2 \theta_s}{2R^2} \left[\frac{2\pi f}{c_0} \sqrt{\mu_r \left(\varepsilon_\infty + \frac{\Delta\varepsilon}{1 + f^2\tau^2} \right)} \right]^4 \left[\frac{\mu_r \left(\varepsilon_\infty + \frac{\Delta\varepsilon}{1 + f^2\tau^2} \right) - 1}{\mu_r \left(\varepsilon_\infty + \frac{\Delta\varepsilon}{1 + f^2\tau^2} \right) + 2} \right]^2 \left(\frac{d}{2} \right)^6 \quad (17)$$

whit R being the distance between the observer and the particle, θ_s represents the angle of scattering, f is the frequency of the electromagnetic signal, c_0 is the velocity of free space, μ_r is the magnetic permeability, ε_∞ is the dielectric constant of the full-polarized medium at an infinite frequency electromagnetic field, $\Delta\varepsilon = \varepsilon_{static} - \varepsilon_\infty$ is the difference between the permittivity values of, respectively, a steady and an infinite frequency electromagnetic field, τ is the relaxation time, and d stands for the diameter of the particle. According to the moisture content, a non-linear modulation of the electromagnetic signal is produced by scattering. In this regard, the author demonstrated how the peak of frequency was a comprehensive indicator, negatively related to moisture. Accordingly, since scattering is caused by water presence in the medium, more scattering events are expected as the moisture content increases.

In line with Equation (17), it was observed how the several frequency components of the frequency spectra were differently scattered, depending on the soil type and water contents, and how the peak of the frequency spectrum f_P was consistent with the frequency component having the maximum scattered intensity of the EM wave. On the basis of several experimental evidences, the following regression law for inferring moisture content θ , expressed in %, from the value of the peak of frequency f_P , expressed in $\text{Hz} \times 10^8$, was proposed:

$$\theta = (A - f_P) / B \quad (18)$$

where A and B are regression parameters calibrated through laboratory tests on different soil samples. In this paper, the RSM was applied to analyse the behavior of clayless and clay-rich soil samples and to provide further insights about moisture content evaluation on the types of soil analysed, according to Equation (18).

EXPERIMENTAL FRAMEWORK

Experimental design

The main purpose of the experimental design is to provide a research scenario wide enough on the EM behavior of clayey soils, outlined by the combination of different-textured soil samples in both clayless and clay-rich conditions along with several moisture content amounts. A detailed description of the samples preparation for this work, including compaction procedures and clay mixing, can be found in Tosti *et al.* 2013. In addition, standard procedures for cross-checking the homogeneous wet conditions within the soil samples have been implemented, as it will be described later.

Test devices and equipment

Experimental tests were carried out using two different GPR systems. In more details, an ultra wideband (UWB) stepped frequency continuous wave (SFCW) radar, was set-up by exploiting a vector network analyzer (VNA) manufactured by Hewlett Packard (8753C, 300 kHz – 3 GHz) to collect data in the frequency domain (Figure 3a). More information on the antenna properties, the calibration procedures, the experimental setup for such type of off-ground measurements, as well as about the dimensions of the test formworks can be found in Tosti *et al.* 2013. In addition to these information, it is worth to mention that the calibrated height of the antenna was fixed at 0.32 m above the sample surface.

Similarly, a pulsed radar system with ground-coupled antennas (pulseEKKO PRO manufactured by Sensors & Software Inc., Canada), 500 MHz center frequency of investigation, was used in a bi-static configuration and common offset (Figure 3b). Data were collected in the time domain, using a 40ns time window and a time step of 5×10^{-2} ns.

FIGURE 3. Test devices and equipment a) SFCW radar set-up using a vector network analyzer HP 8573C (Hewlett Packard Company, USA) and a linear polarized double-ridged broadband TEM horn BBHA 9120 A (Schwarzbeck Mess-Elektronik, Germany), in a mono-static

configuration. b) PulseEKKO PRO 500 pulsed radar system, manufactured by Sensors & Software Inc., Canada.

Materials and laboratory testing

Typical road materials used for unbound pavement layers construction and subgrade soils were used for laboratory testing. In more details, three different soil types, classified by the AASHTO soil classification system as A1, A2, and A3 were considered, being, respectively, gravel (A1, grain size 4-8 mm), coarse sand (A2, grain size 1-2 mm), and fine sand (A3, grain size 0.125-0.250 mm).

Concerning the clay-rich samples, an amount of 15% by weight of bentonite clay was added to the above three types of undisturbed materials. The Colclay A90 bentonite clay, manufactured by Ankerpoort NV, The Netherlands, is mineralogically mainly composed by smectite, consisting of silica (62% by weight) and alumina (21% by weight) sheet-like bounded particles. Mineral thin units get separated by water intrusion between the particles, thereby causing a sudden dispersion of the bentonite in the water.

Increasing amounts of water content were gradually added to the soil samples from dry up to saturated conditions. After the mixing and compaction procedures, the bulk density of each soil sample was collected. To ensure homogeneous moisture conditions within the samples, a number of three samplings was carried out in the barycenter and in the lower and upper corners of the formwork, alongside the diagonal line of the specimens, such that it was possible to determine the average gravimetric water content of each sample after drying in the oven the sampled material. In line with this, it is worth mentioning that a relatively high homogeneity was broadly demonstrated in all the samples by means of low standard deviation values between the aforementioned three sampled VWC amounts (i.e., standard deviation $\sigma_{\theta} < 2\%$). A thorough list of the main physical properties of the dry-member materials used in this work, including bentonite clay, can be found in Tosti *et al.* 2013.

RESULTS AND DISCUSSION

Soil behavior analysis through permittivity-based methods

According to the flowchart of Figure 2, permittivity values ϵ_{TDSF} are firstly estimated from the measured signal in time domain, after implementing the inverse Fourier transform of the measured responses in the frequency domain, sample by sample.

In a second step, the inversion process is run. According to this, each measured signal $G_{xx,mea}^\dagger(\omega)$ is compared with a 3-D matrix of Green's functions $G_{xx,mod}^\dagger(\omega)$, sized $[N \times M \times F]$, being $N = 75$ (i.e., ϵ_r), $M = 60$ (i.e., σ), and $F = 640$ (i.e., number of frequencies collected), with a relatively large parameter space used for running such inversions. As previously mentioned, the target value of ϵ_r can be searched in the parameter space defined by $\pm 10\%$ of the ϵ_{TDSF} value of first approximation. Furthermore, the frequency-dependent electrical conductivity $\sigma(f)$ has been evaluated according to Equation (9), being the parameter space for σ_f variable in the range $[10^{-1} \div 10^{-4} \text{ Sm}^{-1}]$ within a bandwidth B spanning the 1 – 3 GHz frequency range. Finally, the F parameter has been obtained by the ratio between the above cited bandwidth B and an assumed frequency step f_s of 3.125 MHz. It is also worth to mention that the distance h_0 between the equivalent point source of the antenna and the soil sample surface was fixed at 0.32 m, being the equivalent point source located at 0.07 m from the antenna aperture.

Figure 4a,b depicts two examples of measured and modeled responses in the frequency and time domain by FWI application.

FIGURE 4. Measured and modeled Green's functions in the frequency (amplitude $|G_{xx}^\dagger|$ and phase $\angle G_{xx}^\dagger$) and time (g_{xx}^\dagger) domain. (a) soil sample 23 (A3, clay = 0%, $\theta = 10.9\%$); (b) soil sample 45 (A3, clay = 15%, $\theta = 9.7\%$).

As it can be seen in the $|G_{xx}^\dagger|$ plots, a smoother behavior can be observed in case of clay presence (Figure 4b), being the same soil type (i.e., A3) considered in both the figures, with

volumetric water contents comparable each other. Amplitudes for the clayless A3 soil sample (Figure 4a) reach higher peak values than in case of clay. Concerning the Green's functions in the g_{xxx}^T time domain, two main peaks of reflection can be clearly singled out in both these figures. It is also worth to note how signal amplitudes in the time domain can be affected by mismatches occurring in the frequency domain. The comparison between the two g_{xxx}^T plots of Figure 4a,b for the clayless and the clay-rich soil samples shows the positions of the first main peaks of reflection (air-soil interface) at 2.03 ns and 2.02 ns, respectively. Coherently, the second main peaks of reflection (soil/PEC interface) are measured at 3.63 ns and 3.43 ns, thereby providing time distances $\Delta t = 1.60$ ns for (a) and $\Delta t = 1.40$ ns for (b). Such trend can be considered as comprehensive case studies for the overall behavior of the road materials investigated, being the position of the first main peak of reflection approximately the same for all the samples, while the second main position usually locates in floating time distances, as expected by the different physical conditions that were manufactured in the specimens on purposes. It is also worthwhile to note how relatively good matches between permittivity estimates with TDSP and FWI techniques have been found, whereby errors $\leq 8\%$, 7% , and 6% can be detected for A1, A2, and A3 soil types, respectively.

In addition to the above two techniques for permittivity estimation, the SRM was used to retrieve further values of dielectric permittivity ϵ_{SRM} from the measured signal in the time domain relative to each soil sample. On the other hand, permittivity values ϵ_{VMF} from the VMF approach were also inferred by exploiting the physical properties of soil samples along with the moisture contents gravimetrically determined.

Methods comparison

Table 1 lists the values of relative dielectric permittivity assessed by the above four methods in both clayless and clay-rich conditions. As it can be easily observed, the overall trend proves how increasing values of relative dielectric permittivity are reached for higher water amounts in

samples, as expected. In addition to this, considerably lower values of permittivity can be observed in clayey samples, reasonably due to the swelling properties of clay that tightly bound water particles by molecular forces up to higher water abundances, thereby not enabling a full polarization of the water dipoles when the EM field is applied. Clay-rich samples also exhibit permittivity estimates with the four approaches very close each other, with slight variations of permittivity between dry-member and end-member (i.e., saturated) cases. On the contrary, considerable differences of dielectrics are detected in clayless cases both for estimates on same members with the four approaches, and for the permittivity values across the range of moisture investigated.

TABLE 1. Relative dielectric permittivity values retrieved using different methods for 0% and 15% clay samples.

In line with the above, the plots in Figure 5a-f provide interesting insights on the EM response of different textured soils concerning the effects of clay presence in volumetric water content evaluation. For sake of clearness and according to the aforementioned minor errors of permittivity estimates between TDSP and FWI techniques, only dielectrics from the FWI method are taken into account in this analysis. Petrophysical relationships from Topp *et al.* (1980) were then used for best comparing the goodness of the processing techniques employed with the empirical expectations on moisture content estimates. In more details, both the Topp general expression and the Topp site-specific relationship for the Rubicon sandy loam (SL) soil type, with grain size distribution comparable on the average to all the soil types herein analyzed and very low clay contents, were used for the clayless soil samples, while only the Topp general expression was applied to the clay-rich member cases.

Concerning clayless samples behavior (i.e., Figures 5a-c), it can be argued how the agreement of the processing methods in θ estimate is highly dependent on the soil texture. In particular, the lower is the grain size of the material, the similar and closer are the EM responses retrieved. To

broadly quantify the errors between permittivity estimates by different approaches, the Normalized Root Mean Square Deviation (NRMSD) index has been therefore evaluated for each pair combination of methods, as follows:

$$NRMSD = \frac{\sqrt{\frac{\sum_{i=1}^n (\varepsilon_{r_i}^s - \varepsilon_{r_i}^r)^2}{n}}}{\varepsilon_{r_{max}} - \varepsilon_{r_{min}}} \quad (19)$$

where $\varepsilon_{r_i}^s$ and $\varepsilon_{r_i}^r$ are the i^{th} estimated permittivity values for, respectively, the considered and the reference method, n is the number of parameters, $\varepsilon_{r_{max}}$ and $\varepsilon_{r_{min}}$ are, respectively, the maximum and minimum permittivity values within the population of the reference method taken into account. Table 2 lists the NRMSD values for the whole set of processing techniques that have been compared. Such relevant statistics confirm lower distances in permittivity estimates of the A3 soil type, with errors approaching the zero, namely, 0.03 when considering FWI and both the Topp's estimates. On the contrary, these errors increase for higher grain sizes up to 0.84 (i.e., NRMSD value by FWI and Topp (general) comparison for A1 soil samples).

TABLE 2. Normalized Root Mean Square Deviation (NRMSD) values in clayless soil samples by comparing the different permittivity-based methods.

In line with this, experimental tests have highlighted that the greater was the grain size of samples, the more remarkable were the heterogeneities observed in water distribution throughout the volume of the formworks, which in case of the A1 soil type along with relatively low moisture contents began to fall in the occurrence of a free-water layer at the bottom of the test box. This could be reasonably due to a very low threshold of both loosely bound molecular and capillary water which may be formed for this grain size, being the amount of capillary water controlled by the soil texture, soil structure, organic matter and gravity (Lyon and Buckman 1937). Accordingly, capillarity tends to have a greater contribution in finer-textured materials, thereby resulting in much more meniscus around single or multiple particles. It is therefore clear

how different soil properties along with several amounts of moisture reflect in different EM behaviors when applying an EM field. This can be singled out according to the trend of permittivity values retrieved by the FWI with respect to SRM, VMF, and Topp-based approaches. When considering A1 soil samples (Figure 5a) in the gravel size domain, capillarity occurs up to very low volumetric water contents. Indeed, similar estimates can be seen up to $\theta = 2.68\%$, beyond which the FWI begins to return very much higher values of permittivity than the other techniques. In this regard, Scullion and Saarenketo (1997) found very similar correlation between dielectric values and moisture contents of gravel Texas aggregates.

Explanations for this behavior lie on the own theoretical principles of these processing techniques. By experimental evidence, the SRM approach returns relatively flat values of permittivity within the A1 and A2 soil samples, respectively in Figures 5a and 5b, with an increasing trend observed for the last two member-cases of A2 soil samples when the permittivity approaches the analogous estimates by the other processing methods. In line with this, a more regular and slight increasing behavior can be also seen in A3 soil samples (Figure 5c), wherein major effects of capillarity occur. Within this framework, when moisture content increases in coarser-sized materials such as A1 soils, the upper unsaturated volume of the formwork retains the same levels of loosely bound water, while the thickness of the water layer progressively increases at the bottom. Since the SRM strongly relies on surface reflections, the higher is the grain size of soils (i.e., lower amounts of loosely bound and capillary water), the more different will be the values retrieved of permittivity near the soil surface. Such behavior diverts when the depth to water layer approaches the surface, namely, for moisture conditions close to saturation, the SRM approach becomes more sensitive to free water, thereby resulting in higher dielectrics. Where loosely bound water contribution and capillary effects are higher (i.e., finer-textured soils), the SRM returns permittivity values more consistent with the water added to the samples (i.e., A3 soil in Figure 5c).

A certain weak sensitivity to water is instead broadly observed for permittivity estimates using the VMF method, which slightly rise for finer-textured materials. Relying on the theoretical

assumptions of a homogeneous distribution of the multi-phase soil components within each weighted volume and same wave propagation velocity through the medium, the relevant permittivity estimates do not reflect the real distribution of water within the formwork. Such behavior is more emphasized in coarser materials, such as the A1 soil sample than in A2 and A3 soils, where capillary effects contribute at more homogeneously distributing moisture within the multi-phase volume of the specimen.

The FWI approach takes instead into account the whole thickness of the samples, and returns a modeled signal which includes all the possible information of the waveform related to a non-homogeneous distribution of water.

On the other hand, EM behavior in clay-rich soil samples (i.e., Figures 5d-f) is strongly related to the presence and amount of clay particles, which deeply affect how the water molecules adhere to the particle surface. In more details, the water dipole is oriented according to the electrical charge of the clay particle when applying an EM field, by virtue of molecular forces (Benedetto 2010). In this case, a high-density layer of tightly bound water around the particle surface is formed. When moisture content increases, a thicker film of oriented dipoles comes to create, and the outer water changes into the so-called loosely bound layer, since the bonding forces decrease with the distance from the mineral surface. Basically, the aforementioned layers of adsorbed water consist of monomolecular layers which surround negatively charged mineral surfaces and further absorption water layers that can be tightly or loosely bound (Mitchell 1992). In this regard, when clay particles are present and water molecules are bound in the form of adsorbed water, the EM field applied by GPR enables to orientate only the loosely bound water dipoles. When increasing moisture contents, a thicker film of water around the soil particles occur, thereby enabling the polarization of the outer dipoles. This reflects in a lower variability of the soil dielectric properties with water content regardless from a certain considerable amount of θ .

According to the above framework, a very good consistency in permittivity estimates is observed by the application of the FWI and VMF methods within all the three types of soil

investigated, being the NRMSD indexes equal to 0.12, 0.16 and 0.21 for, respectively, A1, A2 and A3 soil samples (Table 4). This is due to fairly homogeneous moisture content conditions throughout the whole thickness of the formwork, so that lower differences between near surface permittivity values by SRM and full-depth dielectrics by FWI occur. In addition to this, it is worthwhile to note how the application of the VMF approach overestimates the ϵ_{VMF} values (i.e., A2 and A3 soils in Figures 5e and 5f), since the water content contribution is completely taken into account by the theoretical model, and the electrical losses due to the rates of tightly bound water to clay particles are not considered.

Overall, the application of Topp general relationship returns considerable overestimated values of dielectric permittivity for all the three types of soil. The VMF approach provides in turn intermediate permittivity estimates in the between of the Topp approach and the above mentioned FWI and SRM. Finally, it should be noted how the best agreement among the several approaches is verified for the A1 soil type (Figure 5d).

FIGURE 5. Plots of volumetric water contents θ vs dielectric permittivity values ϵ_r by different permittivity-based methods in clayless – A1 (a), A2 (b), A3 (c) – and 15% of clay conditions – A1 (d), A2 (e), A3(f) –.

TABLE 3. Normalized Root Mean Square Deviation (NRMSD) values in clay-rich soil samples (15% of clay) by comparing the different permittivity-based methods.

Soil behavior analysis through the Rayleigh scattering method (RSM)

Radar traces from the pulseEKKO pulsed radar system were processed for each test. A denoising step was applied by means of low-pass and high-pass filters. Subsequently, a fast Fourier transform (FFT) was used for retrieving the frequency spectrum of the radar signal, and the frequency peak f_p of each spectrum was then extracted. To enhance the accuracy of the

processing, a number of 20 traces per sample was collected, so that a more stable value of f_p was achieved for each soil sample by averaging as follows:

$$\bar{f}_p = \frac{1}{n} \sum_{i=1}^n f_{p,i} \quad (20)$$

with n being the total amount of i replicas, and $f_{p,i}$ is the frequency of the i^{th} spectrum. Such operation is useful in case of non-unique values of f_p extracted by FFT in the same soil sample, namely, when the shift of the spectrum peak approaches to be sensitive to an increase of water content. Further insights on the application of super-resolution techniques in the spectral domain are discussed in Benedetto and Tosti (2013b).

An overview on the behavior describing the frequency modulations of signal spectra can be seen in Figure 6a-f.

It is evident how the frequency peak moves systematically to lower values of frequency, regardless from the grain size and the presence of clay, which however are fundamental to provide a more comprehensive interpretation of such occurrence. Table 4 lists the measured values of frequency peaks, case by case.

FIGURE 6. 3D representation of the frequency spectra modulation for the soil types investigated from dry to saturated conditions. Clayless conditions – A1 (a), A2 (b), A3 (c) – and 15% of clay conditions – A1 (d), A2 (e), A3(f) –.

TABLE 4. Measured values of frequency spectra peaks f_p [$\text{Hz} \times 10^8$] for 0% and 15% clay samples from dry to saturated conditions.

The overall behavior in both clayless and clay-rich conditions in terms of peaks shifting is represented, respectively, in Figure 7a and 7b. In addition and according to Equation (18), the calibrated A and B parameters along with the relevant regression coefficients for volumetric moisture content prediction are listed in Table 5. As it can be seen, the mean squares fitting

linear curves are characterized by relatively high correlation coefficient R^2 , especially for finer-grained soil types A2 and A3 with 15% of clay content.

FIGURE 7. Trend of values of frequency spectra peak (f_p) across the range of moisture contents investigated for clayless (a), and clay-rich soil samples (b).

TABLE 5. Values of regression coefficients in Equation (18).

Numerical data show how the frequency shift occurs, across the range of moisture investigated, with two main rates of displacement whose dimensions vary according to the grain size and clay content of the samples. Basically, a lower shift of frequency peaks is firstly observed (i.e., low amounts of water content). Secondly (i.e., increasing amounts of water content), more remarkable displacements are noticed.

In both clayless and clay-rich conditions, it can be noticed that the coarser is the grain size of the soil type the lower is the amount of moisture whereby the aforementioned two steps occur. In line with this, when considering clayless conditions (Figure 6a-c), the range of frequency peaks variation Δf_p for the A1 soil type reaches a moisture content of $\theta = 6.71\%$ (Sample 7) when the above second main step of displacement begins (relevant $\Delta f_p_{A1-0\% \text{ clay}} = 4.11 \times 10^8$ Hz). The same step begins at $\theta = 21.43\%$ (Sample 16) for the A2 soil type (relevant $\Delta f_p_{A2-0\% \text{ clay}} = 3.92 \times 10^8$ Hz), while lower displacements are reached for the A3 soil type, being the last moisture value θ equals to 26.63% (Sample 27) with a significantly lower range of variation of frequency peaks (relevant $\Delta f_p_{A3-0\% \text{ clay}} = 2.15 \times 10^8$ Hz).

In clay-rich conditions (Figure 6d-f), numerical results demonstrate how the above occurrence is broadly more attenuated, although its strong dependence on the grain size of soil samples is yet confirmed. Indeed, despite of lower Δf_p intervals, much higher volumetric water contents than in clayless conditions are observed within this range, and the finer is the grain size the higher is the amount of moisture. In more details, such range of variation $\Delta f_p_{A1-15\% \text{ clay}}$ measures 3.14×10^8 Hz for the A1 clay-rich soil type, and it is reached in a wide field of moisture ($\theta = 23.95\% -$

Sample 32). In A2 clay-rich soil samples, the highest $\Delta f_{P_{A2-15\% \text{ clay}}}$ measures 0.59×10^8 Hz with a relevant moisture content $\theta = 27.13\%$ (Sample 41), while $\Delta f_{P_{A3-15\% \text{ clay}}} = 1.57 \times 10^8$ Hz and $\theta = 29.40\%$ (Sample 51) are noticed for the A3 clay-rich finer soil type.

Such overall behavior can find reasonable explanations by relating the contribution of water, clay and grain size of the undisturbed material. Several transition water states occur when starting to add water in a system of dry soil particles, namely, tightly bound and loosely bound adsorption water, capillary water, and free water (Mitchell 1992). According to this, different rates of polarization of the water dipoles occur, with the grain size and mineralogy of soils playing an important role in the modes of such occurrence (Saarenketo 1998). In case of A1 clay-rich soil samples (Figure 6d), the widest experimental heterogeneity between particles from undisturbed material (i.e., grain size 4-8 mm) and bentonite clay is encountered. When adding low amounts of water into a dry system composed by many particles from these two types of population, both the gravel and the clay particles retain water by molecular forces, therefore it is expected that the water dipoles are not fully-polarized by the EM field. In such a condition, lower variations of the frequency peaks of the spectra can be noticed. When increasing the water content, clay particles continue to retain moisture, due to their swelling properties, without undergoing any polarization, while gravel grains begin to loose water molecules, which in contrast start to polarize. In such a condition, slightly higher variation of the frequency peaks of the spectra can be observed. On the other hand, if the water amount added is considerable, both the two types of population take part in the polarization of water dipoles, since a large amount of clay particles begin to polarize all together. Such condition reflects in the highest rate of variation of the frequency spectra peaks, as a result of a sudden amount of polarized water dipoles. In case of finer-grained particles with 15% of clay content, such as the A3 clay-rich soil samples (Figure 6f), the above two populations are characterized by particle sizes very close each other, thereby the A3 fine sand is capable to retain higher amounts of water, as well as to loose more gradually water molecules. In line with this, such “shifting” behavior involving the peaks of frequency spectra is much more attenuated.

Accordingly, when considering clay-less conditions (Figure 6a-c) with a unique soil particle and homogeneous grain size, the shift of the frequency peaks of spectra occurs more rapidly and linearly, although a higher disorder of the several frequency components of the spectra can be broadly observed.

CONCLUSIONS

This study is motivated by the need to understand the dielectric behavior of clayey subgrade soils and unbound load-bearing layers using GPR. GPR data from two different radar systems are analyzed at the laboratory scale of investigation for three types of soil classified by AASHTO as A1, A2, and A3 in both clayless and clay-rich conditions (15% by weight of clay) under different water contents.

Several permittivity-based methods were used for data processing, namely, the time-domain signal picking technique, the full-waveform inversion method, the surface reflection method, and the volumetric mixing formulae. An implementation of the time domain signal picking technique within the full-waveform inversion method has been also presented. Considerably lower values of dielectric permittivity are observed in clayey samples with respect to clayless conditions. Permittivity estimates very close each other are also detected between dry-member and end-member (i.e., saturated) cases by the four approaches. On the contrary, considerable differences of dielectrics are detected in clayless cases both for estimates on same members with the four approaches, and for the permittivity values across the range of moisture investigated. Comparisons between the above dielectrics and the volumetric water content of samples, gravimetrically determined, highlight considerable differences among the full-waveform technique and the other approaches. A very good capability of this method in evaluating permittivity values of unsaturated coarse-grained materials in clayless conditions is shown. Overall, differences in permittivity estimates decrease for finer grain sizes, such that the full-waveform inversion traces relatively well the trend of the Topp general relationship in the A3

soil type. The surface reflection method and the volumetric mixing approach do not perform well in characterizing the volumetric water contents in 10.5cm thick formworks.

Concerning clay-rich soil samples, a very good agreement in the trend of full-waveform inversion and surface reflection methods is noticed, due to the swelling properties of clay, which creates a relatively homogeneous mixtures of the multi-phase components of the soil samples, so that low changes of permittivity throughout the thickness of the formwork are encountered. In such clayey conditions, the Topp general expression broadly overestimates the values of soil permittivity. By a lower entity, considerable overestimates are also encountered using the volumetric mixing approach.

The ability to detect clay in soils was also investigated using a Rayleigh-based scattering technique, which relies on analyses carried out in the spectral domain of the GPR signal. The results demonstrate a strong contribution of water, clay and grain size of the undisturbed material on the occurrence of scattering phenomena. Higher variations in the range of frequency spectra peaks are noticed in clayless soil samples with respect to clay-rich conditions, being this frequency-dependent behavior more rapid and linear, despite of an overall higher disorder of the several frequency components of the spectra. On the contrary, clay-rich soils exhibit tidier spectral behaviors, and frequency shifts develop across higher amounts of water content, due the swelling properties of clay. Soil-specific regression functions are proposed for estimating moisture content as a function of the peaks of frequency spectra.

ACKNOWLEDGEMENTS

The research was supported by the ASTRI project, financed by Roma Tre University under the Framework Program for “Progetto di internazionalizzazione della ricerca e della formazione della ricerca”. A strong support was also provided by the Delft University of Technology, for enabling the use of facilities, materials, and laboratory sites. The authors are thankful to Dr. Karl-Heinz Wolf for permission to use the laboratory sites, as well as to Ing. Karel Heller and Ing. Wim Verwaal, for their invaluable help and support.

This work also benefited from the network activities carried out within the EU funded COST Action TU1208 “Civil Engineering Applications of Ground Penetrating Radar”.

References

- Abdi, M.R., Sadrnejad, A., Arjomand, M.A., 2009. Strength enhancement of clay by encapsulating geogrids in thin layers of sand. *Geotext. Geomembranes*. 27, 447-455.
- Abusharar, S.W., Han, J., 2011. Two-dimensional deep-seated slope stability analysis of embankments over stone column-improved soft clay. *Eng. Geol.* 120, 103-110.
- Al-Qadi I.L. and Lahouar S. 2004. Use of GPR for thickness measurement and quality control of flexible pavements. *Journal of the Association of Asphalt Paving Technologists* 73, 501–528.
- American Association of State Highway and Transportation Officials (AASHTO), 2011. *Roadside Design Guide*, 4th edition. AASHTO, Washington, DC.
- Benedetto A. 2010. Water content evaluation in unsaturated soil using GPR signal analysis in the frequency domain. *Journal of Applied Geophysics* 71, 26–35. doi: 10.1016/j.jappgeo.2010.03.001.
- Benedetto, A., Tosti, F., Di Domenico, L., 2012a. Elliptic model for prediction of deflections induced by a Light Falling Weight Deflectometer. *J. Terramechanics*. 49 (1), 1-12.
- Benedetto A., Benedetto F. and Tosti F. 2012b. GPR applications for geotechnical stability of transportation infrastructures. *Nondestructive Testing And Evaluation* 27(3), 253–262. doi: 10589759.2012.694884.
- Benedetto A., Manacorda G., Simi A. and Tosti F. 2012c. Novel perspectives in bridges inspection using GPR. *Nondestructive Testing And Evaluation* 27(3), 239–251.
- Benedetto A. 2013. A three dimensional approach for tracking cracks in bridges using GPR. *Journal of Applied Geophysics* 97, 37–44. 10.1016/j.jappgeo.2012.12.010.
- Benedetto A., Tosti F., Ortuani B., Giudici M. and Mele M. 2013. Soil Moisture Mapping using GPR for Pavement Applications. In: *Proceedings of the Seventh International Workshop on Advanced Ground Penetrating Radar*, Nantes, France, pp. 243-248. doi: 10.1109/IWAGPR.2013.6601550.
- Benedetto A. and Tosti F. 2013a. Inferring bearing ratio of un-bound materials from dielectric properties using GPR: the case of Runaway Safety Areas. In: *Proceedings of the Airfield and*

- Highway Pavement 2013 Conference*, Los Angeles, California, USA, pp. 1336-1347. doi: 10.1061/9780784413005.113.
- Benedetto A., D'Amico F. and Tosti F. 2014a. Improving safety of runway overrun through the correct numerical evaluation of rutting in Cleared and Graded Areas. *Safety Science* 62, 326–338. doi: 10.1016/j.ssci.2013.09.008.
- Benedetto, A, Tosti, F., Pajewski, L., D'Amico, F., and Kusayanagi, W. 2014b. FDTD Simulation of the GPR Signal for Effective Inspection of Pavement Damages. In: *Proceedings of the Fifteenth International Conference on Ground Penetrating Radar*, Bruxelles, Belgium, pp. 513-518.
- Benedetto F. and Tosti F. 2013b. GPR spectral analysis for clay content evaluation by the frequency shift method. *Journal of Applied Geophysics* 97, 89–96. doi: 10.1016/j.jappgeo.2013.03.012.
- Beroya, M.A.A., Aydin, A., Katzenbach, R., 2009. Insight into the effects of clay mineralogy on the cyclic behavior of silt–clay mixtures. *Eng. Geol.* 106, 154-162.
- Birchack J.R., Gardner C. G., Hipp J.E. and Victor M. 1974. High dielectric constant microwave probes for sensing soil moisture. *Proceedings of the IEEE*. Vol 62. No. 1.
- Bohren CF, Huffman D. *Absorption and scattering of light by small particles*. New York: John Wiley; 1983.
- Chertkov, V.Y., Ravina, I., 2000. Shrinking–swelling phenomenon of clay soils attributed to capillary-crack network. *Theor. Appl. Fract. Mech.* 34, 61-71.
- Chertkov, V.Y., 2005. The shrinkage geometry factor of a soil layer. *Soil Sci. Soc. Am. J.* 69, 1631-1683.
- Daniels D.J. 2004. *Ground Penetrating Radar*. The Institution of Electrical Engineers, London.
- Davis, J.L., Annan, A.P., 2002. Ground penetrating radar to measure soil water content, in Dane, J.H. and Topp, G.C. (eds), *Methods of Soil Analysis, Part 4*, Soil Science Society of America (SSSA), pp. 446-463.

- De Benedetto, D., Castrignano, A., Sollitto, D., Modugno, F., Buttafuoco, G., Papa, G.L., 2012. Integrating geophysical and geostatistical techniques to map the spatial variation of clay. *Geoderma*, 171-172, 53-63.
- Dobson, M.C., Ulaby, F.T., Hallikainen, M.T., El-Rayes, M.A., 1985. Microwave dielectric behavior of wet soil. Part II. Dielectric mixing models. *IEEE Transactions on Geoscience and Remote Sensing* 23, 35–46.
- Drude, P., 1902. *The theory of Optics*. Longmans, Green, and Co, New York, 268–396.
- Dudoignon, P., Causseque, S., Bernard, M., Hallaire, V., Pons, Y., 2007. Vertical porosity profile of a clay-rich marsh soil. *Catena* 70, 480-492.
- Fellner-Feldegg, H., 1969. Measurement of dielectrics in time domain. *The Journal of Physical Chemistry* 73, 616–623.
- Fiori, A., Benedetto, A., Romanelli, M., 2005. Application of the effective medium approximation for determining water contents through GPR in coarse-grained soil materials. *Geophysical Research Letters* 32, L09404.
- Gómez-Ortiz, D., Martín-Crespo, T., Martín-Velázquez, S., Martínez-Pagán, P., Higuera, H., Manzano, M., 2010. Application of ground penetrating radar (GPR) to delineate clay layers in wetlands. A case study in the Soto Grande and Soto Chico watercourses, Doñana (SW Spain). *Journal of Applied Geophysics*, 72 (2), 107-113.
- Gorriti A.G. and Slob E.C. 2005. Synthesis of all known analytical permittivity reconstruction techniques of nonmagnetic materials from reflection and transmission measurements. *IEEE Geoscience and Remote Sensing Letters*, Vol. 2, No. 4, doi: 10.1109/LGRS.2005.853199
- Ho, K.C., Gader, P.D., Wilson, J.N., 2004. Improving landmine detection using frequency domain features from ground penetrating radar. *Proceedings. 2004 IEEE International Geoscience and Remote Sensing Symposium, IGARSS '04*, Vol. 3, pp. 1617–1620.
- Huisman J.A., Hubbard S.S., Redman J.D. and Annan A.P. 2003. Measuring soil water content with ground penetrating radar: a review. *Vadose Zone Journal* 2, 476–491. doi: 10.2113/2.4.476.

- Huston D.R., Hu J., Maser K., Weedon W. and Adam C. 1999. Ground penetrating radar for concrete bridge health monitoring applications. In: *Proceedings of SPIE 3587*, pp. 170-179. doi:10.1117/12.339922.
- Lambot S., Slob E.C., van den Bosch I., Stockbroeckx B. and Vanclooster M. 2004. Modeling of ground-penetrating radar for accurate characterization of subsurface electric properties. *IEEE Transactions on Geoscience and Remote Sensing* 42, 2555–2568. doi: 10.1109/TGRS.2004.834800.
- Lambot S., Weihermüller L., Huisman J.A., Vereecken H., Vanclooster M. and Slob E.C. 2006. Analysis of air-launched ground-penetrating radar techniques to measure the soil surface water content. *Water Resources Research* 42(11), W11403. doi: 10.1029/2006WR005097.
- Lichtenecker, K., Rother, K., 1931. Die herleitung des logarithmischen mischungsgesetzes aus allgemeinen prinzipien der stätionaren strömung. *Physik Z.* 32, 255–260.
- Lyon, T.L., Buckman, H.O., 1937. *The Nature and Properties of Soils*. Macmillan, New York. p. 391.
- Mahmoudzadeh, M.R., André, F., van Wesemael, B., Lambot, S., 2011. Clay content and soil moisture mapping using on-ground time-domain GPR. In *Proceedings of the 2nd Workshop on Proximal Soil Sensing*, Montreal, Canada, May 15-18. p. 44-47.
- Mie, G., 1908. Beiträge zur Optik trüber Medien, speziell kolloidaler Metallösungen. *Annalen der Physik* 330, 377.
- Minet J, Wahyudi A., Bogaert P., Vanclooster M. and Lambot S. 2011. Mapping shallow soil moisture profiles at the field scale using full-waveform inversion of ground penetrating radar data. *Geoderma* 161, 225–237. doi: 10.1016/j.geoderma.2010.12.023.
- Miqueleiz, L., Ramirez, F., Seco, A., Nidzam, R.M., Kinuthia, J.M., Abu Tair, A., Garcia, R., 2012. The use of stabilised Spanish clay soil for sustainable construction materials. *Eng. Geol.* 133-134, 9-15.
- Mitchell, J.K., 1992. *Fundamentals of Soil Behavior*, 2nd edn. Wiley, New York. p. 437.

- Narayana, P.A., Ophir, J., 1983. On the frequency dependence of attenuation in normal and fatty liver. *IEEE Transactions on sonics and ultrasonics* SU30 6, 379–383.
- Odeh, I.O.A., McBratney, A.B., 2000. Using AVHRR images for spatial prediction of clay content in the lower Namoi Valley of eastern Australia. *Geoderma* 97, 237-254.
- Pakbaz, M.S., Alipour, R., 2012. Influence of cement addition on the geotechnical properties of an Iranian clay. *Appl. Clay Sci.* 67-68, 1-4.
- Patriarca C., Tosti F., Velds C., Benedetto A., Lambot S. and Slob E.C. 2013. Frequency dependent electric properties of homogeneous multi-phase lossy media in the ground-penetrating radar frequency range. *Journal of Applied Geophysics* 97, 81–88. doi: 10.1016/j.jappgeo.2013.05.003.
- Redman J., Davis J., Galagedara L. and Parkin G. 2002. Field studies of GPR air launched surface reflectivity measurements of soil water content. In: *Proceedings of the Ninth International Conference on Ground Penetrating Radar*, Santa Barbara, California, USA. S. Koppenjan and K. Lee, Eds. 4758, pp. 156-161.
- Richard, G., Cousin, I., Sillon, J.F., Bruand, A., Guéris, J., 2001. Effect of compaction on the porosity of a silty soil: influence on unsaturated hydraulic properties. *Eur. J. Soil Sci.* 52, 49-58.
- Robinson, D.A., Phillips, C.P., 2001. Crust development in relation to vegetation and agricultural practice on erosion susceptible, dispersive clay soils from central and southern Italy. *Soil Till. Res.* 60, 1-9.
- Robinson, D.A., Campbell, C.S., Hopmans, J.W., Hornbuckle, B.K., Jones, S.B., Knight, R., Ogden, F., Selker, J. Wendroth, O., 2008. Soil moisture measurement for ecological and hydrological watershed-scale observatories: a review. *Vadose Zone Journal* 7 (1), 58–389.
- Roth, K., Schulm, R., Fluhler, H., Attinger, W., 1990. Calibration of time domain reflectometry for water content measurement using composite dielectric approach. *Water Resources Research* 26, 2267–2273.
- Saarenketo, T., 1998. Electrical Properties of Water in Clay and Silty Soils. *Journal of Applied Geophysics* 40(1–3), 73–88.

- Saarenketo, T., Scullion, T., 2000. Road evaluation with ground penetrating radar. *J. Appl. Geophys.*, 43 (2), 119-138.
- Scullion T., Lau C.L. and Chen Y. 1994. Pavement evaluations using ground penetrating radar. International Conference on Ground Penetrating Radar. In: *Proceedings of the Fifth International Conference on Ground Penetrating Radar*, Kitchener, Ontario, Canada, pp. 449-463.
- Scullion, T., Saarenketo, T., 1997. Using suction and dielectric measurements as performance indicators for aggregate base materials. Transportation Research Record 1577, TRB, national Research Council, Washington, D.C., pp. 37-44.
- Serbin G. and Or D. 2004. Ground-penetrating radar measurement of soil water content dynamics using a suspended horn antenna. *IEEE Transactions on Geoscience and Remote Sensing*, Vol. 42, No. 8. doi: 10.1109/TGRS.2004.831693.
- Slob, E.C., Fokkema, J.T., 2002. Interfacial dipoles and radiated energy, *Subsurface Sens. Technol. Appl.*, 3(4), 399 – 419.
- Slob E.C., Sato M. and Olhoeft G., 2010. Surface and borehole ground-penetrating-radar developments. *Geophysics* 75(5), A103-A120. doi: 10.1190/1.3480619.
- Srasra, E., Bergaya, F., Fripiat, J.J., 1994. Infrared spectroscopy study of tetrahedral and octahedral substitutions in an interstratified illite-smectite clay. *Clays and Clay Minerals*, 42 (3), pp. 237-241.
- Topp G.C., Davis J.L. and Annan A.P. 1980. Electromagnetic determination of soil water content: measurements in coaxial transmission lines. *Water Resources Research* 16, 574–582. doi: 10.1029/WR016i003p00574.
- Tosti, F., Benedetto, A., Calvi, A. 2014a. Efficient air-launched ground-penetrating radar inspections in a large-scale road network. In Proc. of the 3rd International Conference on Transportation Infrastructure, Pisa, Italy, Apr. 2014, pp. 703–709.
- Tosti, F., Adabi, S., Pajewski, L., Schettini, G., and Benedetto, A. 2014b. Large-scale analysis of dielectric and mechanical properties of pavement using GPR and LFWD. In: *Proceedings of*

the Fifteenth International Conference on Ground Penetrating Radar, Bruxelles, Belgium, pp. 268-273.

Tosti, F., Umiliaco, A. 2014. FDTD simulation of the GPR signal for preventing the risk of accidents due to pavement damages. *International Journal of Interdisciplinary Telecommunications and Networking* 6(1), pp. 1-9.

Tosti F., Patriarca C., Slob E.C., Benedetto A. and Lambot S. 2013. Clay content evaluation in soils through GPR signal processing. *Journal of Applied Geophysics* 97, 69–80. doi: 10.1016/j.jappgeo.2013.04.006.

Triantafylis, J., Lesch, S.M., 2005. Mapping clay content variation using electromagnetic induction techniques. *Comput. Electron. Agr.* 46, 203-237.

Uzan, J., 1998. Characterization of clayey subgrade materials for mechanistic design of flexible pavements. *Transportation Research Record*, (1629), pp. 189-196.

van der Kruk J. and Slob E.C. 2004. Reduction of reflections from above surface objects in GPR data. *Journal of Applied Geophysics* 55, 271–278. doi: 10.1016/j.jappgeo.2004.02.002.

Viscarra Rossel, R.A., Cattle, S.R., Ortega, A., Fouad, Y., 2009. In situ measurements of soil colour, mineral composition and clay content by vis–NIR spectroscopy. *Geoderma* 150, 253-266.

Voltz, M., Cabidoche, Y.M., 1995. Non-uniform volume and water content change in swelling clay soil: I. Theoretical analysis. *Eur. J. Soil Sci.* 46, 333-343.

Wagner, W., Blöschl, G., Pampaloni, P., Calvet, J.C., Bizzarri, B., Wigneron, J.P., Kerr, Y., 2007. Operational readiness of microwave remote sensing of soil moisture for hydrologic applications. *Nordic Hydrology* 38 (1), 1–20.

Wobshall, D. 1978. A frequency shift dielectric soil moisture sensor. *IEEE Geosci. Electronics*, Vol. GE16, 112-118.

Wuddivira, M.N., Robinson, D.A., Lebron, I., Bréchet, L., Atwell, M., De Caires, S., Oatham, M., Jones, S.B., Abdu, H., Verma, A.K., Tuller, M., 2012. Estimation of soil clay content from hygroscopic water content measurements. *Soil Science Society of America Journal*, 76 (5), pp.

1529-1535.

List of captions

FIGURE 1 Measured Green's function in the time domain $g_{xx,msa}^{\dagger}(t)$ and time delay Δt between air-medium and medium-PEC interfaces.

FIGURE 2. Flowchart representing the implementation of the TDSP technique within the FWI approach.

FIGURE 3. Test devices and equipment a) SFCW radar set-up using a vector network analyzer HP 8573C (Hewlett Packard Company, USA) and a linear polarized double-ridged broadband TEM horn BBHA 9120 A (Schwarzbeck Mess-Elektronik, Germany), in a mono-static configuration. b) PulseEKKO PRO 500 pulsed radar system, manufactured by Sensors & Software Inc., Canada.

TABLE 1. Relative dielectric permittivity values retrieved using different methods for 0% and 15% clay samples.

FIGURE 4. Measured and modeled Green's functions in the frequency (amplitude $|G_{xx}^{\dagger}|$ and phase $\angle G_{xx}^{\dagger}$) and time (g_{xx}^{\dagger}) domain. (a) soil sample 23 (A3, clay = 0%, $\theta = 10.9\%$); (b) soil sample 45 (A3, clay = 15%, $\theta = 9.7\%$).

TABLE 2. Normalized Root Mean Square Deviation (NRMSD) values in clayless soil samples by comparing the different permittivity-based methods.

FIGURE 5. Plots of volumetric water contents θ vs dielectric permittivity values ϵ_r by different permittivity-based methods in clayless – A1 (a), A2 (b), A3 (c) – and 15% of clay conditions – A1 (d), A2 (e), A3(f) –.

TABLE 3. Normalized Root Mean Square Deviation (NRMSD) values in clay-rich soil samples (15% of clay) by comparing the different permittivity-based methods.

FIGURE 6. 3D representation of the frequency spectra modulation for the soil types investigated from dry to saturated conditions. Clayless conditions – A1 (a), A2 (b), A3 (c) – and 15% of clay conditions – A1 (d), A2 (e), A3(f) –.

TABLE 4. Measured values of frequency spectra peaks f_p [$\text{Hz} \times 10^8$] for 0% and 15% clay samples from dry to saturated conditions.

FIGURE 7. Trend of values of frequency spectra peak (f_p) across the range of moisture contents investigated for clayless (a), and clay-rich soil samples (b).

TABLE 5. Values of regression coefficients in Equation (18).

Figures

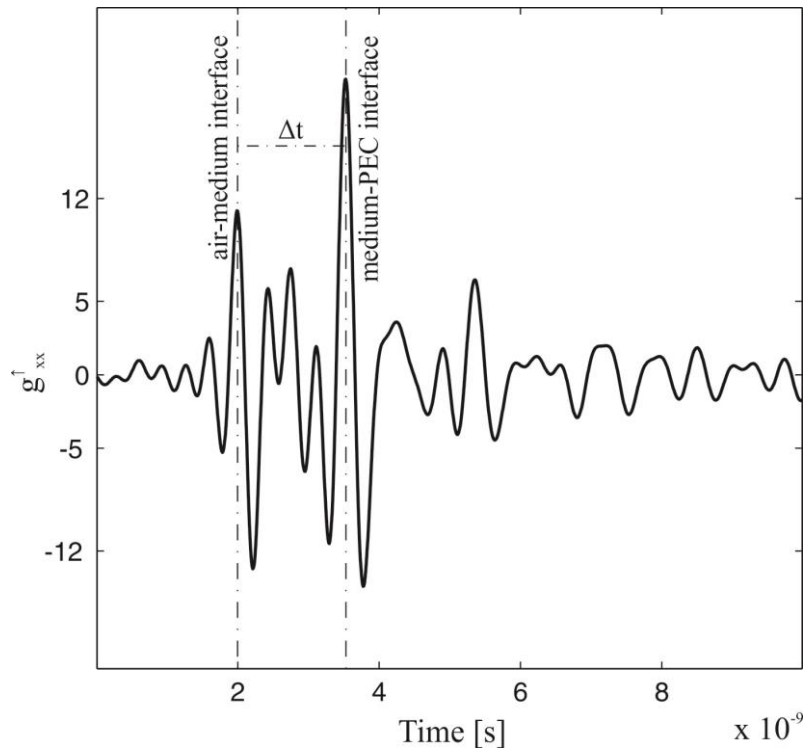


FIGURE 1 Measured Green's function in the time domain $g_{xx,msa}^\dagger(t)$ and time delay Δt between air-medium and medium-PEC interfaces.

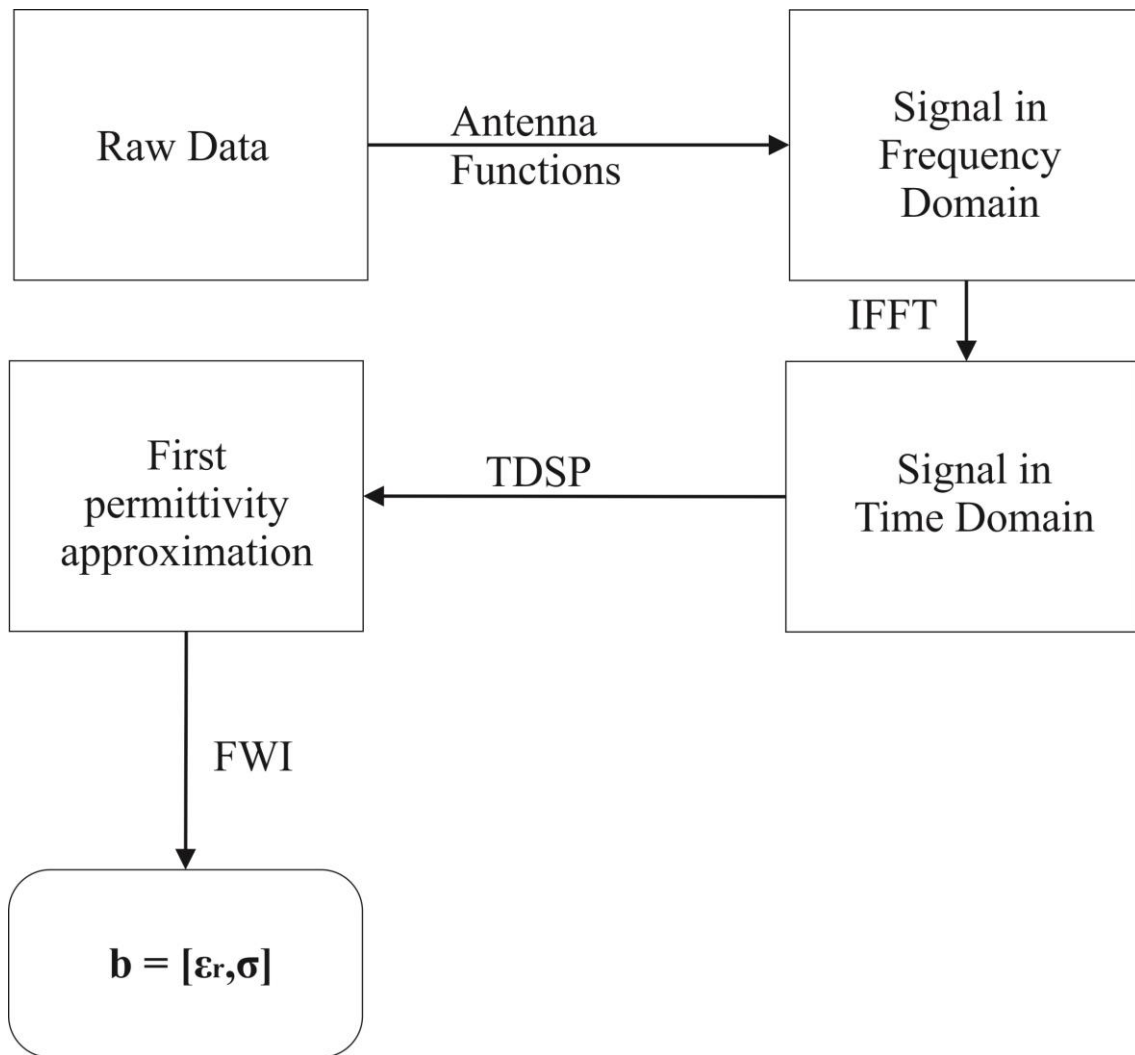


FIGURE 2. Flowchart representing the implementation of the TDSP technique within the FWI approach.



FIGURE 3. Test devices and equipment a) SFCW radar set-up using a vector network analyzer HP 8573C (Hewlett Packard Company, USA) and a linear polarized double-ridged broadband TEM horn BBHA 9120 A (Schwarzbeck Mess-Elektronik, Germany), in a mono-static configuration.



FIGURE 3. Test devices and equipment b) PulseEKKO PRO 500 pulsed radar system, manufactured by Sensors & Software Inc., Canada.

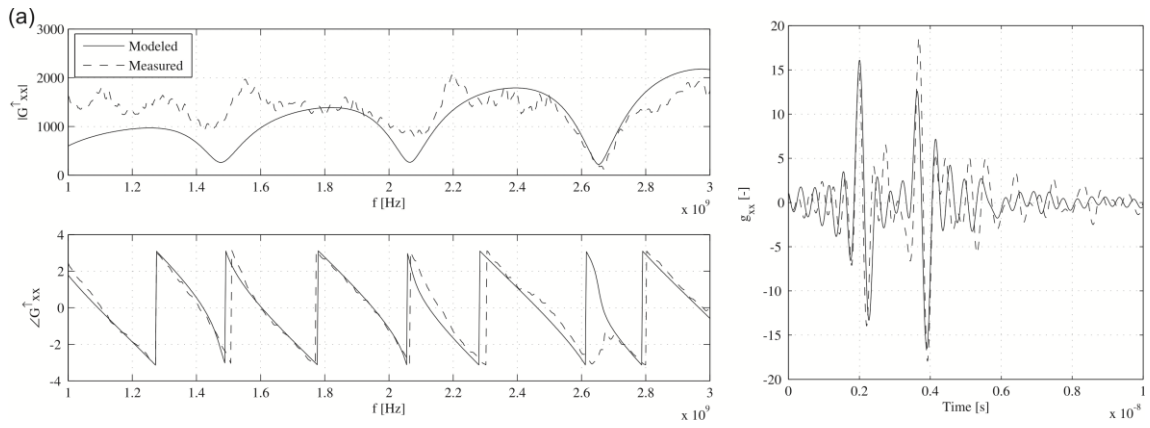


FIGURE 4. Measured and modeled Green's functions in the frequency (amplitude $|G_{xx}^\dagger|$ and phase $\angle G_{xx}^\dagger$) and time (g_{xx}^\dagger) domain. (a) soil sample 23 (A3, clay = 0%, $\theta = 10.9\%$)

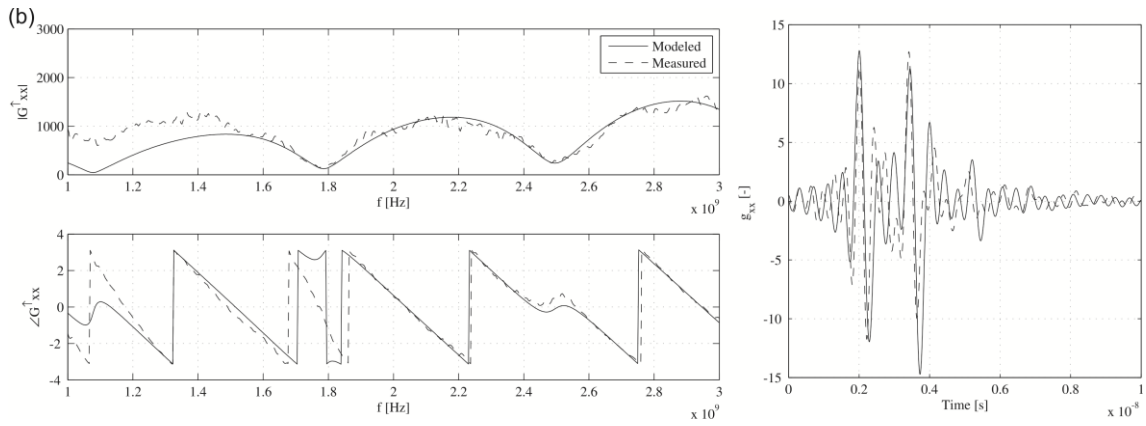


FIGURE 4. Measured and modeled Green's functions in the frequency (amplitude $|G_{xx}^\dagger|$ and phase $\angle G_{xx}^\dagger$) and time (g_{xx}^\dagger) domain. (b) soil sample 45 (A3, clay = 15%, $\theta = 9.7\%$).

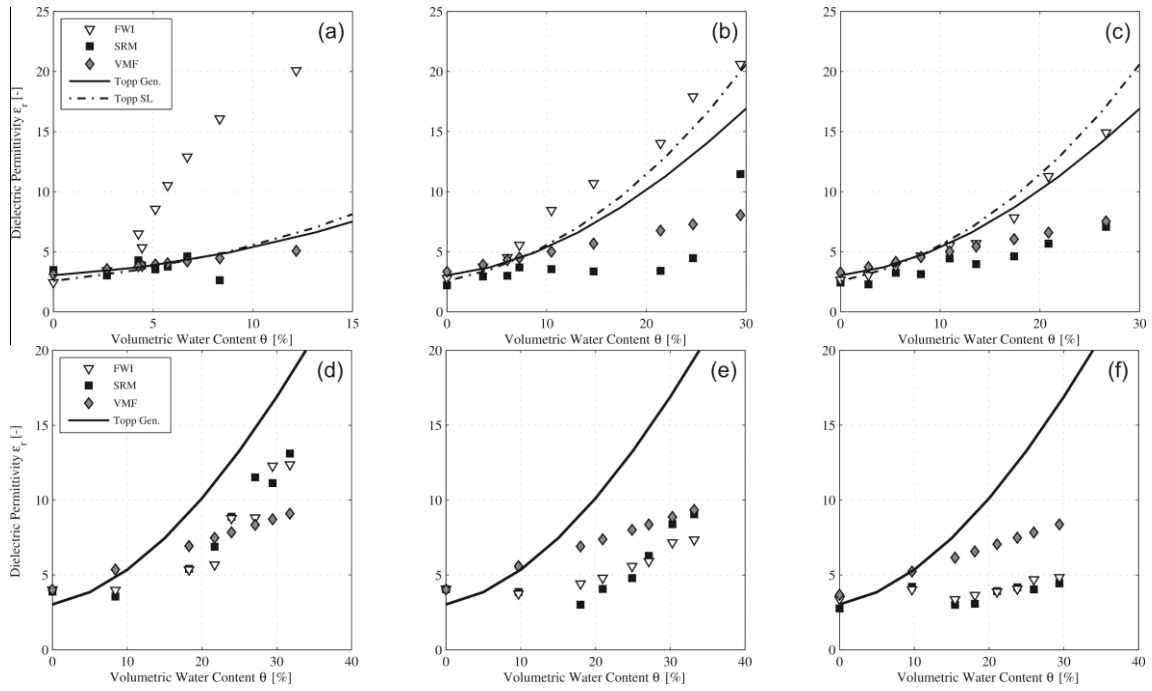
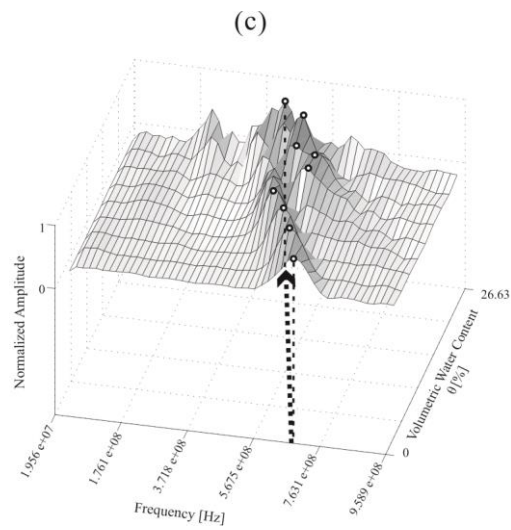
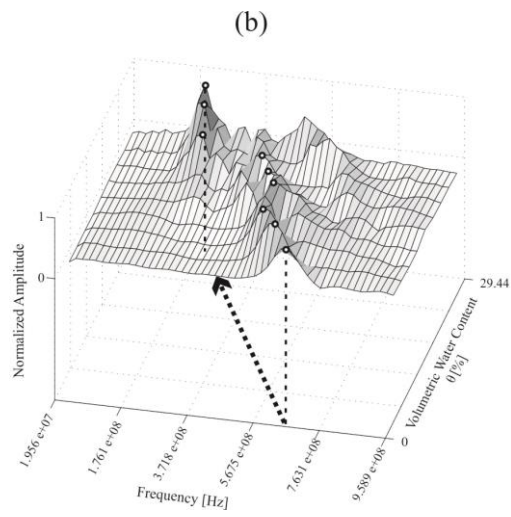
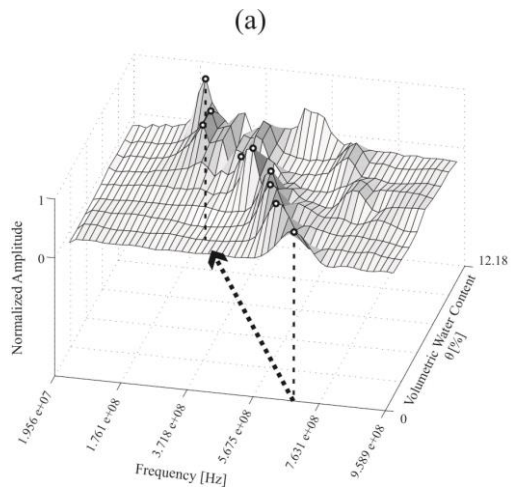


FIGURE 5. Plots of volumetric water contents θ vs dielectric permittivity values ϵ_r by different permittivity-based methods in clayless – A1 (a), A2 (b), A3 (c) – and 15% of clay conditions – A1 (d), A2 (e), A3(f) –.



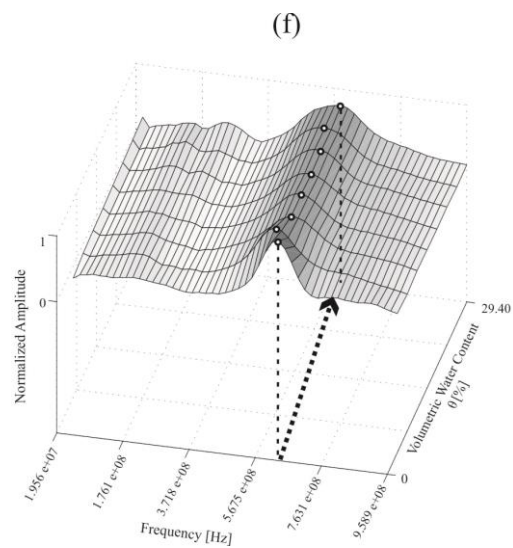
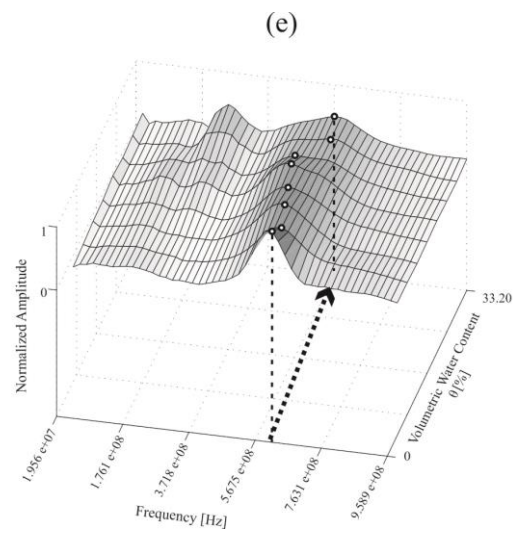
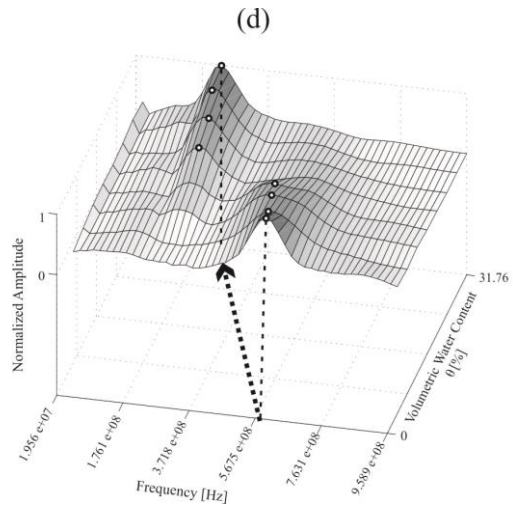


FIGURE 6. 3D representation of the frequency spectra modulation for the soil types investigated from dry to saturated conditions. Clayless conditions – A1 (a), A2 (b), A3 (c) – and 15% of clay conditions – A1 (d), A2 (e), A3(f) –.

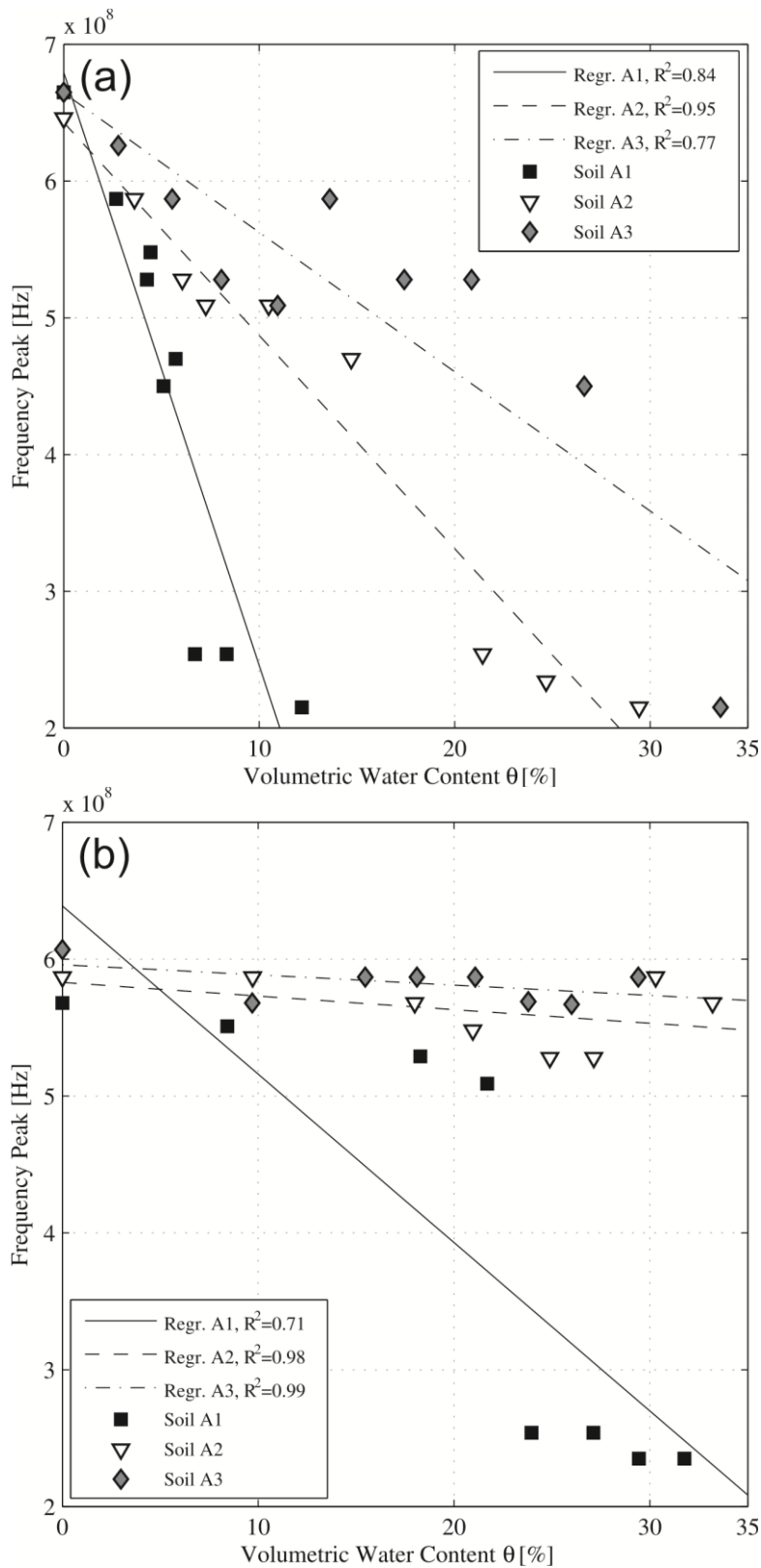


FIGURE 7. Trend of values of frequency spectra peak (f_p) across the range of moisture contents investigated for clayless (a), and clay-rich soil samples (b).

Tables

TABLE 1. Relative dielectric permittivity values retrieved using different methods for 0% and 15% clay samples.

Soil sample ID (0% clay)	θ [%]	ϵ_{TDSP}	ϵ_{FWI}	ϵ_{SRM}	ϵ_{VMF}	Soil sample ID (15% clay)	θ [%]	ϵ_{TDSP}	ϵ_{FWI}	ϵ_{SRM}	ϵ_{VMF}
<i>A1</i>						<i>A1</i>					
Sample 1	0.00	2.53	2.65	3.46	3.12	Sample 28	0.00	3.97	4.02	3.89	4.01
Sample 2	2.68	3.64	3.50	3.02	3.55	Sample 29	8.42	4.32	3.98	3.56	5.36
Sample 3	4.44	5.34	5.30	3.86	3.83	Sample 30	18.27	5.67	5.35	5.41	6.93
Sample 4	4.26	6.42	6.49	4.28	3.80	Sample 31	21.69	6.00	5.68	6.88	7.48
Sample 5	5.11	8.46	8.50	3.53	3.94	Sample 32	23.95	8.63	8.78	8.89	7.84
Sample 6	5.73	10.43	10.52	3.76	4.03	Sample 33	27.11	9.04	8.82	11.52	8.35
Sample 7	6.71	12.9	13.22	4.62	4.19	Sample 34	29.44	12.21	12.28	11.13	8.72
Sample 8	8.34	15.96	16.20	2.63	4.45	Sample 35	31.76	12.30	12.37	13.11	9.09
Sample 9	12.18	20.09	20.59	27.74	5.07						
<i>A2</i>						<i>A2</i>					
Sample 10	0.00	2.74	2.78	2.21	3.33	Sample 36	0.00	4.07	4.06	4.05	4.03
Sample 11	3.62	3.96	3.73	2.94	3.91	Sample 37	9.71	3.91	3.75	3.86	5.58
Sample 12	6.06	4.60	4.52	3.00	4.30	Sample 38	17.99	4.36	4.41	3.02	6.91
Sample 13	7.27	5.93	5.55	3.70	4.50	Sample 39	20.96	4.72	4.80	4.07	7.38
Sample 14	10.48	8.79	8.44	3.56	5.01	Sample 40	24.89	5.47	5.58	4.79	8.01
Sample 15	14.71	11.07	10.69	3.36	5.69	Sample 41	27.13	6.00	5.91	6.28	8.37
Sample 16	21.43	14.44	14.02	3.41	6.76	Sample 42	30.29	6.75	7.16	8.39	8.88
Sample 17	24.68	17.79	17.91	4.47	7.28	Sample 43	33.20	6.85	7.35	9.05	9.34
Sample 18	29.44	21.10	20.60	11.46	8.05						
<i>A3</i>						<i>A3</i>					
Sample 19	0.00	2.64	2.66	2.44	3.26	Sample 44	0.00	3.43	3.38	2.76	3.68
Sample 20	2.80	3.22	3.04	2.28	3.71	Sample 45	9.69	4.02	4.03	4.21	5.23
Sample 21	5.55	3.96	3.80	3.24	4.15	Sample 46	15.46	3.38	3.37	3.01	6.15
Sample 22	8.07	4.84	4.66	3.13	4.55	Sample 47	18.10	3.69	3.65	3.08	6.57
Sample 23	10.95	5.87	5.52	4.45	5.01	Sample 48	21.08	4.02	3.88	3.92	7.05
Sample 24	13.61	6.14	5.69	3.97	5.44	Sample 49	23.79	4.18	4.07	4.17	7.48
Sample 25	17.42	8.06	7.83	4.61	6.05	Sample 50	26.00	4.42	4.69	4.03	7.84
Sample 26	20.87	11.54	11.27	5.67	6.60	Sample 51	29.40	4.65	4.84	4.44	8.38
Sample 27	26.63	15.19	14.91	7.07	7.52						

TABLE 2. Normalized Root Mean Square Deviation (NRMSD) values in clayless soil samples by comparing the different permittivity-based methods.

Methods		NRMSD		
		A1	A2	A3
FWI	SRM	0.44	0.39	0.28
FWI	VMF	0.44	0.56	0.24
SRM	VMF	0.24	0.11	0.21
Topp Gen.	FWI	0.84	0.24	0.03
Topp Gen.	SRM	0.28	0.39	0.40
Topp Gen.	VMF	0.28	0.36	0.38
Topp SL	FWI	0.83	0.11	0.03
Topp SL	SRM	0.33	0.39	0.41
Topp SL	VMF	0.31	0.37	0.38

TABLE 3. Normalized Root Mean Square Deviation (NRMSD) values in clay-rich soil samples (15% of clay) by comparing the different permittivity-based methods.

Methods		NRMSD		
		A1	A2	A3
FWI	SRM	0.12	0.16	0.21
FWI	VMF	0.24	0.37	0.55
SRM	VMF	0.24	0.42	0.54
Topp Gen.	FWI	0.21	0.36	0.46
Topp Gen.	SRM	0.19	0.35	0.47
Topp Gen.	VMF	0.30	0.39	0.43

TABLE 4. Measured values of frequency spectra peaks f_p [$\text{Hz} \times 10^8$] for 0% and 15% clay samples from dry to saturated conditions.

Soil sample ID (0% clay)			Soil sample ID (15% clay)		
sample ID	θ [%]	f_p [$\text{Hz} \times 10^8$]	sample ID	θ [%]	f_p [$\text{Hz} \times 10^8$]
<i>A1</i>			<i>A1</i>		
Sample 1	0.00	6.65	Sample 28	0.00	5.68
Sample 2	2.68	5.87	Sample 29	8.42	5.51
Sample 3	4.44	5.48	Sample 30	18.27	5.29
Sample 4	4.26	5.28	Sample 31	21.69	5.09
Sample 5	5.11	4.50	Sample 32	23.95	2.54
Sample 6	5.73	4.70	Sample 33	27.11	2.54
Sample 7	6.71	2.54	Sample 34	29.44	2.35
Sample 8	8.34	2.54	Sample 35	31.76	2.35
Sample 9	12.18	2.15			
<i>A2</i>			<i>A2</i>		
Sample 10	0.00	6.46	Sample 36	0.00	5.87
Sample 11	3.62	5.87	Sample 37	9.71	5.87
Sample 12	6.06	5.28	Sample 38	17.99	5.68
Sample 13	7.27	5.09	Sample 39	20.96	5.48
Sample 14	10.48	5.09	Sample 40	24.89	5.28
Sample 15	14.71	4.70	Sample 41	27.13	5.28
Sample 16	21.43	2.54	Sample 42	30.29	5.87
Sample 17	24.68	2.34	Sample 43	33.20	5.68
Sample 18	29.44	2.15			
<i>A3</i>			<i>A3</i>		
Sample 19	0.00	6.65	Sample 44	0.00	6.07
Sample 20	2.80	6.26	Sample 45	9.69	5.68
Sample 21	5.55	5.87	Sample 46	15.46	5.87
Sample 22	8.07	5.28	Sample 47	18.10	5.87
Sample 23	10.95	5.09	Sample 48	21.08	5.87
Sample 24	13.61	5.87	Sample 49	23.79	5.69
Sample 25	17.42	5.28	Sample 50	26.00	5.67
Sample 26	20.87	5.28	Sample 51	29.40	4.50
Sample 27	26.63	4.50			

TABLE 5. Values of regression coefficients in Equation (18).

Clay Content [%]	Parameter	Soil		
		A1	A2	A3
0	$A \times 10^8$	6.79	6.43	6.64
	$B \times 10^7$	4.34	1.56	1.02
	R^2	0.84	0.95	0.77
15	$A \times 10^8$	6.34	5.83	5.96
	$B \times 10^7$	1.23	0.10	0.07
	R^2	0.71	0.98	0.99